Biomaterials 197 (2019) 86–100

Contents lists available at ScienceDirect

Biomaterials

journal homepage: www.elsevier.com/locate/biomaterials

Hierarchically targetable polysaccharide-coated solid lipid nanoparticles as an oral chemo/thermotherapy delivery system for local treatment of colon cancer

Ming-Yin Shen[a,b,1], Te-I Liu[a,1], Ting-Wei Yu[a], Reesha Kv[a], Wen-Hsuan Chiang[c], Yuan-Chung Tsai[a], Hsin-Hung Chen[c], Sung-Chyr Lin[c], Hsin-Cheng Chiu[a,*]

[a] Department of Biomedical Engineering and Environmental Sciences, National Tsing Hua University, Hsinchu 300, Taiwan
[b] Department of Surgery, National Taiwan University Hospital-Hsinchu Branch, Hsinchu 30013, Taiwan
[c] Department of Chemical Engineering, National Chung Hsing University, Taichung 402, Taiwan

ARTICLE INFO

Keywords:
Local colon cancer treatment
Hierarchical targeting
Combination therapy
Solid lipid nanoparticles
Oral formulations

ABSTRACT

Although oral formulations of anticancer chemotherapies are clinically available, the therapeutic action relies mostly on drug absorption, being inevitably accompanied with systemic side effects. It is thus desirable to develop oral therapy systems for the local treatment of colon cancers featured with highly selective delivery to cancer cells and minimized systemic drug absorption. The present study demonstrates the effective accumulation and cell uptake of the doxorubicin and superparamagnetic iron oxide nanoparticles-loaded solid lipid nanoparticle (SLN) delivery system for chemo/magnetothermal combination therapy at tumors by hierarchical targeting of folate (FA) and dextran coated on SLN surfaces in a sequential layer-by-layer manner. Both the *in vitro* and *in vivo* characterizations strongly confirmed that the dextran shells on SLN surfaces not only retarded the cellular transport of the FA-coated SLNs by the proton-coupled FA transporter on brush border membranes in small intestine, but also enhanced the particle residence in colon by specific association with dextranase. The enzymatic degradation and removal of dextran coating led to the exposure of the FA residues, thereby further facilitating the cellular-level targeting and uptake of the SLNs by the receptor-mediated endocytosis. The evaluation of the *in vivo* antitumor efficacy of the hierarchically targetable SLN therapy system by oral administration showed the effective inhibition of primary colon tumors and peritoneal metastasis in terms of the ascites volume and tumor nodule number and size, along with the absence of systemic side effects.

1. Introduction

Colorectal cancer is one of the most prevalent malignant neoplasms worldwide. The treatment of colorectal cancer relies mostly on surgery and chemotherapy. The latter becomes more indispensable for cancers at the late stages (stages 3 and 4) featuring the occurrence of local and systemic metastasis, respectively. Currently, most clinically available chemotherapies adopted for the treatment of colorectal cancers are generally administered via intravenous (iv) infusion [1–3]. Except for capecitabine (Xeloda® Tablet) and uracil-tegafur (5-FU) [4,5], the clinically used chemotherapy products developed in oral formulation are rather rare although the administration route is of the highest patient acceptance and compliance among different formulations. This is ascribed to the limited and unsteady drug adsorption in gastrointestinal (GI) tract and the first pass effect on drug metabolism by liver, in close association with the reduction of therapeutic antitumor effect from oral formulations [6–8]. Furthermore, the chemotherapy in oral formulation acting locally on colorectal cancers with negligible systemic absorption and transportation is not yet clinically available owing to the short and erratic duration of the residence at tumor sites and the poor uptake of small molecular drugs by cancer cells [9].

Numerous efforts have been made to demonstrate the profound *in vitro* cytotoxic effect of nanoparticle (NP)-based therapy systems against colon cancer cells and the preferred *in vivo* accumulation and sound antitumor efficacy upon subcutaneous tumor-bearing animal models [10–12]. In spite of increased accumulation at solid tumors by virtue of the enhanced permeation and retention (EPR) effects usually via iv injection due to the neovascular angiogenesis, the NP-based

* Corresponding author.
E-mail address: hscchiu@mx.nthu.edu.tw (H.-C. Chiu).
[1] These authors contributed equally to this work.

https://doi.org/10.1016/j.biomaterials.2019.01.019
Received 18 September 2018; Received in revised form 8 January 2019; Accepted 8 January 2019
Available online 09 January 2019
0142-9612/

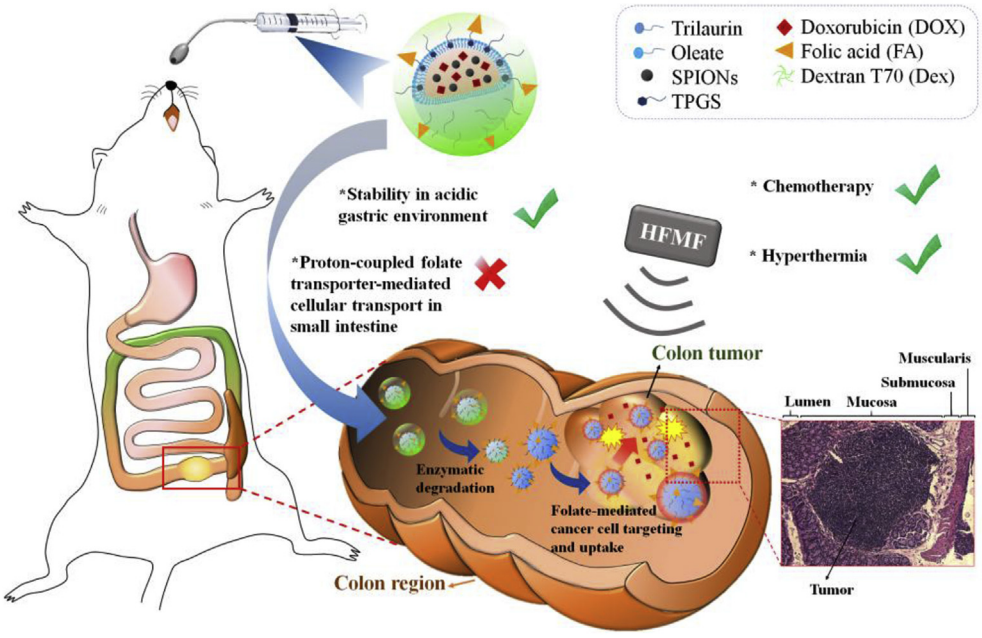

Fig. 1. Schematic illustration of the hierarchically targetable SLN system for the local chemo/thermo combination therapy against colon cancer by oral administration.

therapy delivery systems adopted for parenteral administration for the treatment of orthotopic colon cancer were scarcely reported. Similarly, the reports on the development of NP therapy systems in oral dosage form for orthotropic colorectal cancer treatment are rather few. Hasani-Sadrabadi et al. have prepared Eudragit-coated chitosan-based NPs by a dual cross-junction microfluidic device in an oral paclitaxel formulation for the treatment of colorectal cancer [13]. The drug release was controlled by pH variations with the GI tract in virtue of the dissolution of Eudragit at neutral pH and the swelling of chitosan core under mild acidic conditions. However, further *in vivo* studies are required to demonstrate the improvement in systemic drug adsorption and in antitumor efficacy against colorectal cancer. Vong et al. have developed a redox NP system for oral therapeutics delivery toward orthotopic colitis-associated colon cancer [14]. The NPs contained nitroxide radicals capable of serving as the scavenger of reactive oxygen species (ROS) at the tumor sites and therefore significantly suppressed tumor growth. The antitumor efficacy of the redox NPs against colon cancer was apparently induced with the onset of the NP uptake by tumor cells in the GI tract, without systemic adsorption and transportation [14]. Further studies on the redox NPs (administered by oral gavage) in combination with free doxorubicin (DOX, by iv injection) showed significantly improved antitumor effect for the treatment of orthotropic colon cancer and appreciably reduced adverse side effects caused by the excessive production of ROS from chemotherapy [15].

Considering factors, such as the lack of drug targeting, low bioavailability, erratic retention and severe adverse side effects, expectedly associated with local treatments of chemotherapy against colon cancer [16], the NP-based therapy systems may be a prominent solution to the dilemma described above as the systems are constructed to reduce premature drug leakage and enhance selective tumor targeting and accumulation [17]. It is now recognized that the endocytic pathway of epithelial cells as the outer lining of the GI tract is severely limited by the complementary binding of cadherin with intracellular p120 catenin [18–20]. By contrast, such a binding in colon cancer cells even though transformed from inflammation bowel diseases is relieved, thus restoring the ability of endocytosis, the major underlying pathway for the cellular uptake of NPs for effective local treatment. The fluctuation of the retention time resulting from the inherent entrapment and clearance actions of highly viscoelastic and adhesive mucous layer can also be alleviated by pertinent NP surface modifications [21,22]. Moreover, the mucous layer at tumor areas in colon has been found appreciably removed [23,24], therefore facilitating the endocytic uptake of NPs by cancer cells. Surface decoration of the NP-based therapy systems with appropriate targeting ligands may further enhance tumor accumulation of NPs and selective uptake by cancer cells [25–27], for instance, via receptor-mediated endocytosis. While the latter is usually achieved by the selection of ligands pertinent to receptors present on cancer cell membranes, the enhanced NP accumulation in colon may also be attained by adoption of the colon local environment, for example, with the abundant bacterial flora, distinct from other parts of the GI tract [28,29].

Solid lipid NPs (SLNs) have been considered as a highly promising nanovehicle system particularly for the oral delivery of hydrophobic drugs due to their excellent biocompatibility and structural assistance in drug uptake [30]. In this study, the NP-based chemo/magnetothermal combination therapy system for oral delivery and local treatment of colon cancer was developed. The SLNs loaded with DOX and superparamagnetic iron oxide nanoparticles (SPIONs) were surface modified in sequence with folic acid (FA)/D-α-tocopheryl polyethylene glycol 1000 succinate (FA-TPGS) adduct and octadecanol modified dextran (Oct-Dex) in a layer-by-layer manner. SPIONs were adopted to generate hyperthermia therapy herein, yet not for MRI T_2 imaging. The local combination treatment from both DOX chemotherapy and hyperthermia therapy upon the activation of SPIONs with high-frequency magnetic field (HFMF) were employed against orthotopic colon cancer for the synergistic antitumor effect while the tissue damage of major organs could be significantly reduced owing to the lack of systemic adsorption of the SLNs into blood circulation. Incorporating FA-TPGS onto particle surfaces enables the good dispersion of NPs in aqueous phase and the targeting of NPs to the FA receptor (FAR)-overexpressed cancer cells. Although it has been reported that proton-coupled folate transporters exist on brush border membranes of microvilli in small intestine [31,32], the issue can be fully addressed by the coating of the polysaccharide layers on the NP surfaces that prevents the biorecognization of FA residues on nanocarriers by FA transporters. The octadecanol-modified dextran coated on NP outer surfaces not only reduces the FAR-mediated transportation through brush border membranes in small intestine, but also provides the complementary

association of dextran with dextranase, a bacteria-produced glucanohydrolase present exclusively in colon. Upon enzymatic degradation of dextran, the exposure of the FA residues on NP surfaces acting as the targeting ligands leads to the enhanced uptake of NPs by the FAR-overexpressed cancer cells via receptor-mediated endocytosis. The schematic of the hierarchically targeted NP-based oral delivery strategy for the local treatment of colon cancer is illustrated in Fig. 1. In addition to the structural and morphologic characterization of the SLN-based chemo/thermal combination therapy system, the *in vitro* cellular interactions and the *in vivo* NP distribution along the GI tract and anti-tumor effect against orthotropic colon cancer (CT26) were examined in this work.

2. Materials and methods

2.1. Materials

1-Octadecanol (Oct), carbonyldiimidazole (CDI), 4-dimethylaminopyridine (DMAP), glycidyl methacrylate (GMA), dextran T70 (Dex), dicyclohexylcarbodiimide (DCC), folic acid (FA), ammonium peroxodisulfates (APS), N,N,N′,N′-tetramethylethylenediamine (TMEDA), D-α-tocopheryl polyethylene glycol 1000 succinate (TPGS), and sodium oleate were obtained from Sigma-Aldrich. Doxorubicin (DOX) was purchased from Seedchem (Melbourne, Australia). Oleic acid-coated superparamagnetic iron oxide nanoparticles (SPIONs) were synthesized and characterized as reported previously [33]. All organic solvents were purchased from Alfa Aesar. Deionized water was produced by the Milli-Q Synthesis System (18 MΩ, Millipore). All chemicals were reagent grade and used as received. For cell culture studies, Dulbecco's modified Eagle's medium (DMEM), RPMI 1640 Medium, fetal bovine serum (FBS), 0.25% trypsin–EDTA solution and penicillin–streptomycin solution were purchased from Thermo Fisher Scientific (Waltham, MA, USA). CT26 (murine colon adenocarcinoma cell line), A549 (human lung adenocarcinoma cell line) and 4T1 (murine mammary carcinoma cell line) were obtained from Food Industry Research and Development Institute (Hsinchu City, Taiwan). The 6- to 8-week-old BALB/cByJNarl male mice were purchased from the National Laboratory Animal Center, Taiwan. Approved guidelines for the care and use of laboratory animals by the Institutional Animal Care and Use Committee (IACUC: 10129) were followed throughout the study. Surgeries were performed under Zoletil-Rompun anesthesia, and all efforts were taken to minimize animal suffering [40].

2.2. Syntheses of Oct-Dex and Oct/MA-Dex

Oct-Dex was prepared by CDI coupling reaction. First, Oct (1.0 g) was dissolved in chloroform (5.0 mL). CDI in 4-fold molar excess was added to the solution under stirring for 48 h. The side product, CI, was removed by repeated extraction with deionized water. Chloroform was then evaporated and Oct-CI dried *in vacuo*. Oct-CI (225 mg) and DMAP (76 mg) were added to the Dex solution in DMSO (1.0 g/10 mL) under stirring. The reaction was carried out at 130 °C for 8 h. The crude product was subjected to dialysis (Ordial D14b, MWCO 12,000-14,000, Organic Scientific) against DMSO at 25 °C for 5 days and then deionized water at 4 °C for 3 days. The final product was collected by lyophilization. The structures of Oct-CI and Oct-Dex were confirmed by ^{1}H NMR in d-chloroform and DMSO-d_6, respectively, at the ambient temperature (Fig. S1). Based on the relative integral ratio of the characteristic peak of the anomeric proton from Dex at δ 4.7 ppm to that of the methyl protons from Oct at δ 0.8 ppm, the degree of substitution (DS) defined hereinafter as the number of the conjugated moieties per 100 anhydroglucoside residues was estimated to be ca 8.45 [34,35].

To prepare methacrylate (MA)-containing Oct-Dex (Oct/MA-Dex), MA-Dex was first synthesized as reported elsewhere [34]. In brief, GMA and DMAP were added to the Dex solution in DMSO. The reaction was carried out at room temperature for 48 h under stirring. The reaction was stopped by adding an equimolar amount of concentrated HCl to neutralize DMAP. The MA-Dex was purified by dialysis against deionized water at 4 °C for 5 days and collected by lyophilization. The DS of MA conjugated with Dex was evaluated by ^{1}H NMR in DMSO-d_6 at ambient temperature (Fig. S2a) [34,36–39]. Oct/MA-Dex was prepared by the conjugation reaction of MA-Dex with Oct-CI in a similar manner to Oct-Dex. The DS values of MA and OCT in Oct/MA-Dex were determined by ^{1}H NMR from the relative integral ratios of the characteristic peak of anomeric protons of Dex at δ 4.7 ppm to that of the methyl protons of the Oct residues at δ 0.8 ppm and to that of the alkene protons of the MA residues at δ 5.7 and 6.1 ppm (Fig. S2b). The DS values of Oct and MA were 7.4 and 3.7, respectively.

2.3. Synthesis of FA-TPGS

FA-TPGS was synthesized by Steglich esterification. TPGS (0.2 g) was dissolved in anhydrous DMSO (10 mL) at 40 °C. FA (in 5-fold molar excess with respect to TPGS), DCC (in 8-fold molar excess) and DMAP (equimolar) were added in sequence and the reaction was carried out under stirring at 40 °C for 5 days. The crude product was filtered (0.45 μm PTFE filter) to remove dicyclohexylurea. The reaction solution was dialyzed (MWCO 1000) against DMSO for 5 days and then deionized water for another 5 days at room temperature. The product was collected by lyophilization and the structure examined by ^{1}H NMR in DMSO-d_6. The conjugation efficiency (42.7%) was obtained from the relative integral ratio of aromatic protons from FA at δ 1.8 ppm to methyl protons of TPGS at 0.8 ppm (Fig. S3).

2.4. Enzymatic degradation of modified dextrans

Native dextran, Oct-Dex and Oct/MA-Dex (2.0 mg/mL) were separately dissolved in citrate buffer (pH 5.5). Dextranase (1 mg) was added to the solutions (1.0 mL) under stirring at 37 °C for 4 h. The degradation of native and modified dextrans was examined by gel permeation chromatography (GPC) (PL aquagel-OH 40 8 μm) using citrate buffer as the eluent at a flow rate of 1.0 mL/min under RI detection.

2.5. NP preparation

The SLNs were prepared by the emulsion technique. Trilaurin (24 mg), TPGS (2.0 mg), and SPIONs (2.0 mg) were dissolved in chloroform (700 μL) serving as the organic phase. The aqueous solution (deionized water, 300 μL) containing DOX (0.4 mg) and sodium oleate (11.2 mg) was added dropwise into the organic phase. With the mixture being homogenized by ultrasonication for 10 min in an ice bath, phosphate buffer (pH 7.4, ionic strength 10 mM, 2.5 mL) was added and the mixture was further subjected to the second homogenization by ultrasonication for 10 min. Chloroform in the emulsion was removed by rotary evaporation. The unencapsulated DOX was removed by dialysis against pH 7.4 phosphate buffer for 5 days (MWCO 12,000–14,000). The DOX-loaded SLNs coated with TPGS referred to hereinafter as TSLNs were obtained. Instead of TPGS, FA-TPGS was employed for preparation of DOX-loaded FA-TPGS-coated SLNs (FSLNs). To further modify NP surfaces with dextran, The Oct-Dex solution in DMSO (8.0 mg/100 μL) was added dropwise into the emulsions in the second homogenization process, leading to the production of both dextran-coated TSLNs (abbreviated as DTSLNs) and FSLNs (DFSLNs). To prepare surface dextran-crosslinked SLNs, instead of Oct-Dex, Oct/MA-Dex that provides pendent methacrylate groups for dextran crosslinking was employed for surface coating of nanoparticles. The radical polymerization was then carried out by addition of APS and TMEDA as the initiator system in phosphate buffer into the Oct/MA-Dex coated TSLNs (or FSLNs) suspension under stirring at room temperature. The aqueous solution was dialyzed (MWCO 50,000) against phosphate buffer for 3 days to remove residual APS and TMEDA and side products. The surface dextran-crosslinked samples were referred to as cDTSLNs and cDFSLNs

in this study.

To determine drug loading, the SLNs were dissolved in the mixture of ethanol and aqueous HCl solution (ethanol/HCl (1 N) = 3:1 v/v). The drug loading content was evaluated by measuring the fluorescence intensity at 560 nm (microplate reader, FLUOstar, OPTIMA, BGM Labtech, Germany), following the excitation at 480 nm. The destruction of nanoparticle structure was confirmed by dynamic light scattering. Drug loading efficiency and loading content were estimated according to the following formulas:

Drug loading efficiency (%) = (weight of loaded DOX/weight of DOX in feed) x 100%

Drug loading content (%) = (weight of loaded DOX/weight of the nanoparticles) x 100%

2.6. Structural characterization

The measurements of the hydrodynamic diameter (D_h), size distribution in terms of polydispersity index (PDI), and ξ-potential of different SLNs were conducted on a Malvern Zetasizer Nano-ZS Instrument.

2.7. Colloidal stability of nanoparticles in gastrointestinal environment

Simulated gastric fluid (SGF), simulated intestinal fluid (SIF), and simulated colonic fluid (SCF) were prepared as reported elsewhere [40]. The recipes are shown below. SGF: 0.2 g NaCl, 7.0 mL HCl (1.0 N) in deionized water to a total volume of 1.0 L (pH 1.2); SIF: 6.8 g KH_2PO_4, 0.896 g NaOH in deionized water to a total volume of 1.0 L (pH 6.8); SCG: 0.2 g KCl, 8.0 g NaCl, 0.24 g KH_2PO_4, 1.44 g Na_2HPO_4 in deionized water to a total volume of 1.0 L (pH 7.0). The NP suspensions were diluted 50-fold with SGF, SIF, and SCF, respectively, followed by incubation at 37 °C for 8 h. The particle size was examined at the prescribed time intervals by DLS.

2.8. In vitro drug release

Taking into account of the average residence times of food in stomach, small intestine and colon along the GI tract in mouse model [41], the aqueous dispersion of the drug-loaded SLNs was placed in dialysis bag (MWCO 12,000-14,000) and dialyzed against SGF for first 2 h, SIF for another 2 h, and finally SCF for 4 h. At the prescribed time intervals, the dialysate (0.6 mL) was withdrawn and replaced with the same amount of fresh medium. The concentration of DOX was determined using the microplate reader as previously described in aqueous solution of either SGF, SIF or SCF.

2.9. Magnetothermal evaluation

The aqueous SLN dispersion was placed in 1.5 mL cuvette and treated with HFMF for 9 min. The temperature was recorded every minute with an infrared thermal imaging apparatus (Ti100, Fluke, USA). Phosphate buffer was used as the blank control.

2.10. Cellular uptake

Cancer cells (CT26, 4T1, and A549) were seeded to each well of a 6-well plate (3.5×10^5 cells/well), and incubated for 1 day at 37 °C (5% CO_2). In addition to the CT26 colon cancer cells, the 4T1 breast carcinoma cells that highly express FARs were selected as the positive control. The A549 lung carcinoma was used as the FAR-negative cell line model. Cells were incubated with SLNs at a DOX concentration of 10 μM for 2 h. The various dextran-coated SLNs pretreated with dextranase were also employed. After the cells being washed twice with PBS, DMSO was added into each well for cell lysis. The intracellular DOX level was quantitatively determined by the microplate reader. For the cellular uptake examination by laser scanning confocal microscopy (LSCM), cancer cells seeded on $22 \times 22\ mm^2$ glass coverslips in 6-well plate at 3×10^5 cells/well were incubated at 37 °C for 24 h. The cells were co-incubated with SLNs for 1 h and washed twice with PBS. The cell nucleus and F-actin of cytoskeleton were stained with Hoechst 33342 and CytoPainter F-actin Staining Kit-Green Fluorescence, respectively. The distribution of DOX in cancer cells was examined on a ZEISS LSM-780 LSCM with the excitation wavelength of 488 nm and the emission wavelength of 560 nm.

2.11. Cytotoxicity

Cancer cells were seeded into 96-well plates at a concentration of 5×10^3 cells/well in 0.2 mL RPMI, containing 10% FBS and 1% penicillin, and incubated at 37 °C overnight in an atmosphere of 5% CO_2. SLNs with the prescribed DOX concentrations were added and the co-incubation proceeded for 4 h. After being washed twice with PBS, cells were re-incubated for another 24 h. The MTT solution (10 μL, 5.0 mg/mL) was added into each well and the reaction was carried out for 4 h at 37 °C. The culture medium was then replaced with DMSO (100 μL) and the absorbance at 570 nm was determined using a microplate reader. The *in vitro* anticancer effect from magnetic hyperthermia of the SLNs under HFMF treatment was also examined. Cancer cells were seeded in 24-well plates at a concentration of 1×10^4 cells/well and incubated at 37 °C overnight. SLNs were added and co-incubated for 4 h. After being washed twice with PBS, the cells in fresh culture medium (0.2 mL) were treated with HFMF for 7 min and then re-incubated for another 24 h. The cell viability was examined by MTT assay. To evaluate the synergistic effect of the chemo/thermal combination therapy of the SLNs, drug-free TSLNs of varying Fe concentrations (for hyperthermia), free DOX of varying concentrations (for chemotherapy), and dextranase-pretreated DFSLNs (or DTSLNs) for combination therapy were added and co-incubated with the CT26 cancer cells (24-well, 1 × 104 cells/well) for 4 h, respectively. After being washed twice with PBS, the cells in fresh culture medium (0.2 mL) were treated with HFMF for 7 min (in the hyperthermia and the combination therapy groups) and then re-incubated for another 24 h. The cytotoxicity was examined by MTT assay, followed by calculation of the CI value with CompuSyn software as reported elsewhere [42]. The combination index (CI) values and the CI-versus-Fraction affected (Fa) plots were thus obtained.

2.12. NP distribution in GI tract and tumor growth inhibition

An orthotopic colon tumor model was established as reported previously with slight modification [43]. In brief, the CT26 colon cancer cells at a concentration of 5×10^5 cells in PBS (20 μL) were injected into the colon walls at ca 1 cm beneath the cecum with the aid of surgery that slightly open the abdomens of the BALB/C mice. After inoculation, the wound was sutured to avoid infection. For the distribution study in the GI tract, SLNs were labeled with an NIR probe, DiI, to facilitate the IVIS fluorescence detection (Xenogen IVIS system). After being inoculated with the cancer cells for 7 days, mice were orally administered respectively with TSLN, DTSLN, FSLN and DFSLN by gavage. The mice were sacrificed 6 h post oral administration and the small intestine and colon were collected for the ex vivo IVIS imaging (DiI filter: λ_{ex} = 435 nm; λ_{em} = 640 nm). The mean signal intensity was obtained by dividing the total signal intensity from regions of interest (ROIs) with the number of groups. The DOX concentration within the tumor and normal colorectal tissues were quantified as reported previously with slight modification [44]. The tumor and normal colorectal areas (0.1 g of each) were harvested, wet-weighed and homogenized in 0.5 mL of lysis buffer (0.25 M sucrose, 40 mM tris acetate, 10 mM EDTA) on a VCX-750 Ultrasonic Processor. For DOX measurements, tissue lysate (200 μL) was mixed with Titron X-100 (10%, 100 μL). After being sonicated and vortexed, the extraction solution (1 mL, 1.25 M HCl in 2-propanol) was added and the samples were incubated at −20 °C overnight. After centrifugation at 24,000 g for

20 min, the fluorescence intensity of DOX in the supernatant was measured. The DOX amount was thus obtained from the calibration of the fluorescence intensity of DOX with seven concentrations in HCl/propanol solution.

For the *in vivo* tumor inhibition study, mice were randomly allocated into 8 groups (5 mice per group) at day 6 post tumor inoculation and treated by gavage with PBS (blank control), TSLNs, FSLNs, DFSLNs, TSLN/HFMF, FSLN/HFMF, and DFSLN/HFMF, respectively, at a daily DOX dosage of 12 mg/kg for a total of three doses. To generate hyperthermia effect, the HFMF treatment was performed for 7 min at 6 h post gavage while the mice were under anesthesia via inhalation of oxygen-isoflurane. The body weights of the mice were determined daily for 14 days. Afterward, the mice were sacrificed and the tumor tissues in colon collected. The tumor tissues were weighed and the therapeutic efficacy was evaluated. The metastasis of colon cancer to peritonea (i.e., peritoneal carcinomatosis colorectal cancer (pcCRC)) was examined upon the mouse sacrifice and the murine carcinosis index (MCI) was evaluated as described previously with appropriate modifications [45]. The MCI was defined herein as follows:

$$MCI = \Sigma \text{ (Nodule Diameter Score x Nodule Number Score)}$$

where the tumor nodule diameter score is attained by the nodule size (0 for no visible; 1 for $<$ 0.5 mm; 5 for 0.5 to $<$ 2 mm; 10 for $>$ 2 mm in diameter) and the nodule number score is evaluated by the various ranges of nodule numbers (1 for nodule number 1–5; 2 for 6–10; 3 for 11–15; 4 for 16–20; 5 for 21–25; 6 for $>$ 25).

2.13. Systemic toxicity evaluation

The systemic toxicity of the therapeutic SLNs through oral administration was evaluated in treated tumor-bearing mice in terms of the levels of blood alkaline phosphatase (ALP) and aspartate aminotransferase (ALT). Blood (0.1 mL) withdrawn from orbital sinus of the mice at day 7 and 14 after the first therapeutic treatment was mixed with lithium heparin and the sample was analyzed for ALP and ALT on a Clinical Analyzer AmiShield VCA-TC-100 (ProtectLife International Biomedical Inc).

2.14. H&E examination and IHC analysis

For H&E histologic tissue examination, the major organs, including heart, liver, spleen, lung, kidney, small intestine, colon and tumor, were harvested upon the sacrifice of the tumor-bearing mice at day 14 after the administration of the therapeutic NP along with the HFMF treatment, if applicable. The organs and tumors were embedded in OCT compound (Sakura Finetek, Torrance, CA, U.S.A.) and stored at −80 °C for further H&E staining. The tissue sections (10 μm in thickness) were mounted onto slides and the tissue slides were then fixed with precooled methanol for 5 min and washed twice with PBS. Tissue sections were then stained with H&E and examined under optical microscopy. For tissue IHC examination, the intestines and colons were harvested at day 3 post therapeutic treatment. To prevent nonspecific binding of antibodies, tissue slides were blocked with the protein blocking buffer containing 4% FBS, 1% normal goat serum, and 0.01% Tween-20 in PBS for 1 h at 4 °C. The slides were subsequently incubated with rat antimouse caspase-3 antibodies (BD Pharmingen) at 4 °C. After 24 h, the slides were washed and incubated with the FITC conjugated secondary antibodies (Invitrogen) for 1 h at room temperature. After being washed thoroughly with PBS, the slides were stained with Hoechst 33342 (2.5 μg/mL; Invitrogen) to identify the loci of cell nuclei. Images were captured with the LSCM. The percentage of caspase-3 positive area was obtained from the ratio of the caspase-3 positive area to the total cell (Hoechst positive) area. The normalized caspase-3 intensity was obtained by normalizing the caspase-3 marker fluorescence intensity with Hoechst fluorescence intensity from each SLN group (including the PBS group as a control). The quantification of fluorescence intensity or area was performed with ImagePro Plus software.

2.15. Statistical analysis

All experiments were performed in triplicate unless stated otherwise, and data were reported as mean ± standard deviation. Statistical analysis was performed with Prism 5.0 software (GraphPad Software) by an unpaired two-tailed *t*-test and one-way ANOVA with Bonferroni multiple comparisons. Statistical significance is indicated as (n.s.) $P > 0.05$, (*) $P < 0.05$, (**) $P < 0.005$ and (***) $P < 0.001$.

3. Results and discussion

3.1. Characterization of dual-targeted dextran-coated SLNs

In order to attain the hierarchically dual targeting NP carrier system for oral chemo/thermal combination therapy of colon cancer, the SLNs loaded with DOX and SPIONs (SLNs) were prepared by the emulsion technique and further surface modified in sequence with FA-TPGS and Oct-Dex (or Oct/MA-Dex) in a layer-by-layer architecture. The synthetic routes and ^{1}H NMR structural characterizations of FA-TPGS and Oct-Dex (or Oct/MA-Dex) are illustrated in Figs. S1–S3. The TSLNs, the TPGS-coated SLNs, were ca 100 nm in mean hydrodynamic diameter (D_h) and −30 mV in zeta potential owing to the presence of oleic acid on particle surfaces. It was presumed that the PEG chain segments and the α-tocopherol (vitamin E) residues of TPGS could enhance the colloidal stability of NPs in aqueous phases and enable its anchoring within SLNs by hydrophobic interactions, respectively. The FSLNs, FA-TPGS coated SLNs, exhibited similar size, surface charge density and DOX/SPION loading efficiency to TSLNs as shown in Table 1. Further surface modification of FSLNs (TSLNs) with Oct-Dex by means of hydrophobic embedding of aliphatic chain segments within SLNs gave rise to DFSLNs (DTSLNs) with an increase in particle size from 95 (99) to 132 (144) nm and a decrease in zeta potential from −29.6 (−29.9) to −13.0 (−13.9) mV. The loading efficiencies of DOX were above 80% while the loading contents were in the range 8–10 wt% for all the SLNs

Table 1
DLS data and drug/Fe_3O_4 loading characteristics of SLNs.

Sample	Size (D_h, nm)[a]	PdI	DOX		LC of Fe_3O_4 (wt%)	Zeta potential (mV)
			LE (%)	LC (wt%)		
TSLNs	99.4 ± 8.5[b]	0.142	81.9 ± 4.9	9.78 ± 1.08	0.780 ± 0.106	−29.90 ± 6.67
DTSLNs	144.0 ± 11.8	0.257	89.8 ± 9.2	8.52 ± 0.32	0.700 ± 0.081	−13.90 ± 1.32
cDTSLNs	161.1 ± 1.7	0.192	74.8 ± 0.1	5.58 ± 0.61	0.650 ± 0.075	−15.20 ± 1.39
FSLNs	95.3 ± 3.9	0.130	92.8 ± 9.2	10.4 ± 0.86	0.670 ± 0.206	−29.60 ± 3.60
DFSLNs	132.1 ± 8.7	0.254	92.1 ± 5.9	9.27 ± 0.57	0.720 ± 0.156	−13.00 ± 1.65
cDFSLNs	207.7 ± 39.2	0.294	80.4 ± 6.0	4.83 ± 0.94	0.670 ± 0.145	−15.20 ± 1.01

[a] DLS measurement was performed in phosphate buffer (pH 7.4, I = 0.1 M) at 25 °C.
[b] Error bars represent mean ± s.d (n ≥ 10).

without the cross-linked dextran shell. Two polysaccharide shell cross-linked NPs, namely cDTSLNs and cDFSLNs, were also obtained in an attempt to enhance colloidal stability and protect interior solid lipid cores from enzymatic degradation by intestinal lipases at the upper part of the GI tract. The introduction of MA groups onto dextran renders the polysaccharide to readily undergo cross-linking by radical polymerization of the pendent MA residues in aqueous phase at ambient temperature using APS and TMEDA as the initiation system [34]. With the cross-linked polysaccharide shells, the DOX loading efficiencies (ca 75% for cDTSLNs and 80% for cDFSLNs) were somewhat reduced (Table 1), possibly owing to an additional dialysis step for the removal of APS and TMEDA. An increase in particle size was also observed most likely because of the partial inter-particulate connections during the cross-linking reaction. The DLS hydrodynamic size distribution profiles of various SLNs developed herein are illustrated in Fig. S4 and their properties with respect to particle size, polydispersity and drug loading are summarized in Table 1.

Owing to appreciable variations in pH and salt concentration in stomach, small intestine and colon (rectum) along the GI tract, the colloidal stability of the SLNs was examined in terms of the size variation with time in various simulated fluids. As shown in Fig. S5, the results demonstrate that the particle sizes of the SLNs attained in this work remained essentially unchanged over a time period of 8 h irrespective of the simulated medium, suggesting that these NPs are highly resistant to hydrolysis even in severe acidic gastric environment (pH 1.2) with well-preserved structures. The enzymatic degradability of Oct-Dex and Oct/MA-Dex adducts by dextranase was evaluated in terms of the molecular size change by GPC. As shown in Fig. S6, after 4-h enzymatic reaction, the molecular peak of native (unmodified) dextran in the GPC profile almost entirely disappeared, indicating that dextran was degraded extensively. The enzymatic degradability of dextran was somewhat reduced upon modification with the aliphatic octyl chains and was further decreased by additional conjugation with methacrylate residues, apparently owing to the disruption of the enzyme-substrate interactions by the chemical conjugations. The extent of enzymatic cleavage of Oct-Dex and Oct/MA-Dex was controlled by the DS values of Oct-Dex (8.5) and Oct/MA-Dex (7.4 and 3.7). It has been reported that the six consecutive unmodified glucopyranose residues in dextran are essential for the interaction with dextranase to undergo proper enzymatic action [46,47]. In agreement with the results from the enzymatic cleavage of Oct-Dex by dextranase, the incubation of DTSLNs and DFSLNs with dextranase for 60 min led to the reduction of nanoparticle sizes in D_h to ca 97 nm, similar to the sizes of FSLNs and TSLNs (Fig. 2a). Fig. 2b illustrates the changes of various SLNs in particle size before and after the enzymatic reaction with dextranase for 60 min in SCF. The gel layer formed on the surface via radical polymerization of the MA units significantly reduced the extent of enzymatic cleavage of cDFSLNs and cDTSLNs by dextranase, resulting in only a slight reduction in particle sizes, suggesting that the cross-linked dextran shells still remained on the SLN surfaces after exposure to dextranase. As expected, dextranase exerted little influence on the structure of the dextran-free FSLNs and TSLNs as the particle size remained essentially unchanged after enzymatic reaction for 60 min. It should be noted that the hydrodynamic sizes of the SLNs varied in phosphate buffer and SCF (Table 1 and Fig. 2), which probably could be ascribed to the difference in ionic strength, leading to salt-induced condensation on NP surfaces although the mechanism is not well clarified.

The oral therapeutics delivery strategy developed herein emphasized on the enhanced selective uptake of NPs by cancer cells at colon in the GI tract by virtue of the hierarchical dual targeting and FAR-mediated endocytosis for intracellular drug release and therapeutic action. Therefore, the DOX release from the SLNs prior to transportation along GI tract to the targeted site was considered as a premature drug leakage owing to the lack of drug targeting. The *in vitro* cumulative release of DOX from various SLNs in SGF, SIF and SCF at 37 °C by the dialysis technique in a sequential manner over the time periods of 2 h, 2 h and 20 h, respectively, simulating the residence times in mouse model, was examined. As shown in Fig. S7, slow DOX release profiles, ca 22% for FSLNs and DFSLNs and 10% for TSLNs and DTSLNs, were attained over the entire time interval of 24 h. The difference is attributed to the π-π stacking between FA residues and DOX species that enhances DOX accumulation at particle surfaces and unloading at the initial stage [48,49]. The slowest DOX release was observed from the dextran-crosslinked NPs owing to the presence of the surface gel layer as a penetration barrier to the drug species. The HFMF-induced high temperature effect on the *in vitro* drug release from the SLNs was quite negligible (< 3%) as shown in Fig. S8. Even with the medium temperature being elevated above the melting temperature of trilaurin (ca 47 °C), the drug release from the SPIONs-loaded SLNs is still rather limited. The mechanism underlying the slow DOX (DOX/oleate complexes) release behavior from the SLNs containing the oleic acid-coated SPIONs is not clear, yet most likely being closely associated with the enhanced hydrophobic association. Nevertheless, the intracellular drug release can easily occur via lipid degradation in endosomes/lysosomes or cytoplasm. The loading contents of SPIONs within different SLNs, evaluated by ICP-MS, were ca 0.7 wt%. The oleic acid-coated SPIONs

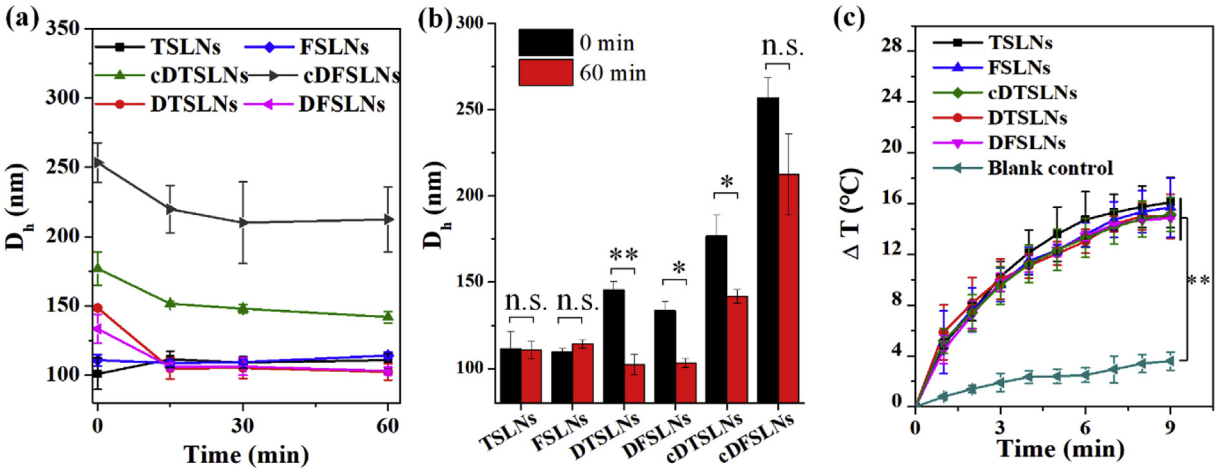

Fig. 2. (a) Time-evolved mean particle sizes (D_h) of various SLNs co-incubated with dextranase in SCF at 37 °C. (b) Variation in mean particle size of various SLNs before and after dextranase reaction over a 60-min time interval. (c) Temperature rise profiles of various SLNs treated with high frequency magnetic field (HFMF) for 9 min. Phosphate buffer was used as the blank control. Samples were analyzed with one-way ANOVA, followed by Bonferroni correction for multiple comparisons. $^{**}P < 0.01$, $^{*}P < 0.05$ and n.s. $P > 0.05$. Error bars represent mean ± s.d (n = 8).

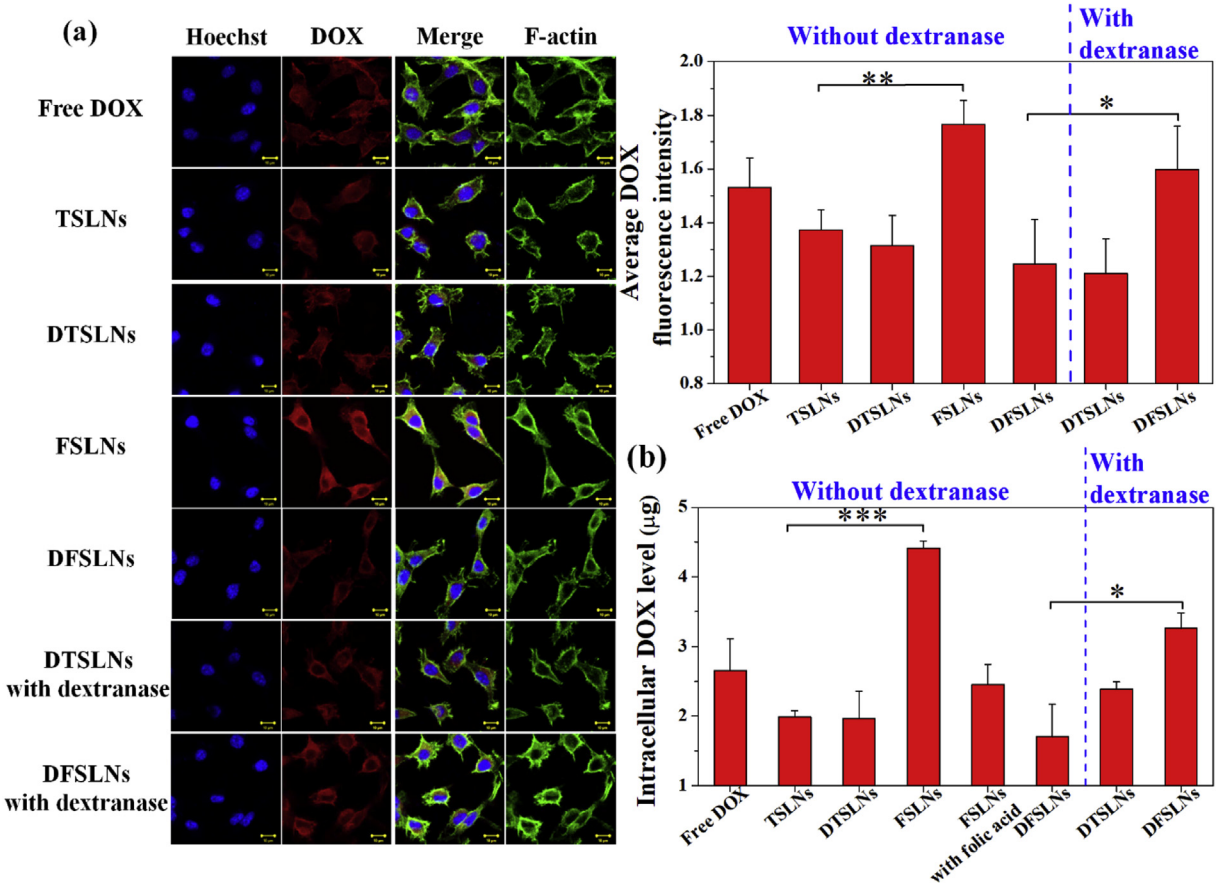

Fig. 3. (a) LSCM images of the cellular uptake of DOX from various SLNs by CT26 colorectal cancer cells. Free DOX was used as a control. F-actin and nucleus were stained in green and blue, respectively. Scale bars are 20 μm. The average DOX fluorescence intensity was analyzed by Image J (n = 10). (b) Intracellular DOX level in CT26 cells after co-incubation with various SLNs (n = 8). The DOX level was determined by fluorescence intensity measurements following cell lysis in DMSO. Samples were analyzed with one-way ANOVA, followed by Bonferroni correction for multiple comparisons. ***$P < 0.001$, **$P < 0.01$ and *$P < 0.05$. Error bars represent mean ± s.d. (For interpretation of the references to color in this figure legend, the reader is referred to the Web version of this article.)

synthesized were characterized by DLS, TGA and SQUID. The results are shown in Fig. S9. The capability of the SLNs with entrapped SPIONs to undergo alternating magnetic field-induced hyperthermia was investigated. As revealed in Fig. 2c, an appreciable temperature elevation of ca 14 °C was observed for all SLN formulations in response to the HFMF treatment for 7 min, indicating the potential of the formulations for thermal therapy in cancer treatment.

3.2. *In vitro cellular uptake of dual targeting NPs*

The *in vitro* targeting efficiency of the FA-decorated SLNs to FAR-overexpressing cancer cells was evaluated in terms of their cellular uptake by mouse colon CT26 cancer cells compared to that of the FA-free SLNs by LSCM examination. The intracellular DOX fluorescence intensity was adopted as a measure for the NP uptake by CT26 cancer cells. Fig. 3a shows the fluorescence imaging of the cancer cells after co-incubation with various SLNs. It is apparent that the uptake of FSLNs by the FAR-overexpressing CT26 cells was substantially enhanced compared to TSLNs and two dextran-coated NPs (DFSLNs and DTSLNs). The intracellular FSLN fluorescence intensity, also shown in Fig. 3a, is even higher (ca 30%) than that of free DOX in spite of different cellular entry pathways. It has been recognized that the cellular entry of free DOX relies on passive diffusion across cell membranes while the FA receptor-mediated endocytosis is the major route for the engulfment of the FA-functionalized nanoconstructs by FAR-overexpressing cells [50,51]. The reduction of cellular uptake of DFSLNs compared to FSLNs was caused by the shielding effect with dextran coating on particle surfaces that impaired the FA-mediated interactions between the NPs and the cells. As a consequence, after the removal of dextran coating with the enzymatic action of dextranase, the DFSLNs showed comparable uptake by CT26 cells to FSLNs. The results also suggest the successful sheltering effect of dextran coating on the FA moieties to serve as a targeting ligand prior to exposure to dextranase. By contrast, irrespective of the dextranase pretreatment, the cellular uptake of cDTSLNs and cDFSLNs was significantly retarded as shown in Fig. S10. In agreement with the data from the enzymatic cleavage of cross-linked dextran shells on NP surfaces (Fig. 2), the reduced cellular uptake of cDTSLNs and cDFSLNs pretreated with dextranase was ascribed primarily to the incomplete cleavage and disruption of surface dextran layers, which hence remained intact in preventing the interaction between NP and the cells, leading to poor cellular uptake of the dextran shell crosslinked SLNs by the cancer cells even at the targeted site. Therefore, the NPs with cross-linked dextran shells were thus not further investigated for the development of oral therapeutics delivery for local colon cancer treatment. The intracellular DOX levels of the CT26 cells after co-incubation with various SLNs were also evaluated spectrometrically in a more precise manner with the cells being completely lysed in DMSO. The results (Fig. 3b) clearly demonstrate again the capability of FA on NP surfaces to promote the cellular NP uptake by the FAR-overexpressing CT26 cells via FAR-mediated endocytosis meanwhile the pronounced sequestering of the FA residues by dextran coating from recognition by CT26 cells was observed. Fig. 4 further shows the uptake of NPs by FAR-overexpressing 4T1 and FAR-negative A549 cancer cells via determination of the DOX fluorescence intensity by the LSCM examination of the

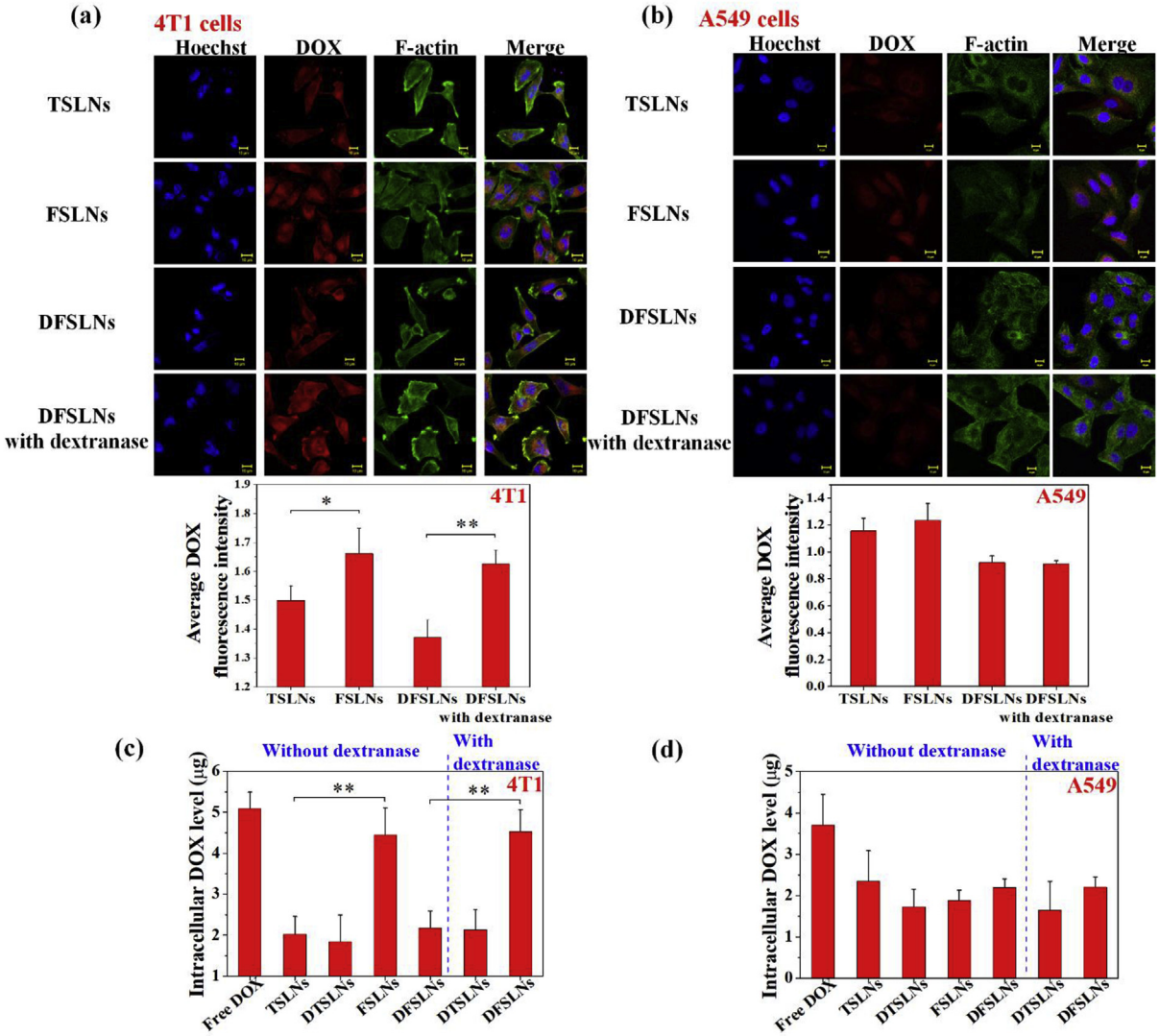

Fig. 4. LSCM images of the cellular uptake of DOX from various SLNs by (a) FAR-overexpressing 4T1 murine breast cancer cells and (b) FAR-negative A549 murine lung cancer cells. Free DOX was used as a control. The average DOX fluorescence intensity was evaluated by Image J ($n \geq 10$). Scale bars are 20 μm. Intracellular DOX levels of (c) 4T1 cells and (d) A549 cells after co-incubation with various SLNs. The DOX level was obtained by quantifying the DOX fluorescence intensity after cell lysis in DMSO ($n = 6$). Samples were analyzed with one-way ANOVA, followed by Bonferroni correction for multiple comparisons. $^{*}P < 0.05$ and $^{**}P < 0.01$. Error bars represent mean ± s.d.

SLNs-engulfed cancer cells and by fluorescence spectroscopic measurements with cell lysis in DMSO, respectively. The intracellular DOX fluorescence intensities of FSLNs and dextranase-pretreated DFSLNs within 4T1 cells were substantially enhanced compared to TSLNs and DFSLNs without dextranase treatment, due to the increased cellular internalization of the NPs by the FAR-mediated endocytosis triggered by the complementary FA/FAR binding. By contrast, the uptakes of TSLNs, FSLNs, DTSLNs and DFSLNs by A549 cells were comparable irrespective of the dextranase treatment, because of the lack of the FAR on A549 cell membranes.

3.3. *In vitro* cytotoxicity

The cytotoxicity of drug-free SLNs against CT26 cancer cells was examined by MTT assay. As revealed in Fig. S11, the DOX-free NPs with or without dextran coating exhibited essentially nontoxic nature toward CT26 cells at an NP concentration of 0.15 mg/mL. The *in vitro* anticancer effects of the NP formulations by means of hyperthermia, chemotherapy and combination therapy against CT26 colon cancer cells were further investigated. For the hyperthermia effect on cancer necrosis, the necrosis of CT26 cells after coincubation with DOX-free NPs and the HFMF treatment was examined by propidium iodide (PI) staining in red while cell nuclei were stained with Hoechst 33342 in blue as shown in Fig. 5a. The cancer cells underwent necrosis to the highest extent upon sequential treatment with DOX-free FSLNs and HFMF because of the enhanced cellular uptake of the NPs by FAR-mediated endocytosis compared to those with DOX-free TSLNs, DTSLNs and DFSLNs. The cytotoxic effect of chemotherapy from various SLNs against CT26 cancer cells was evaluated in terms of the IC_{50} values measured by the extent of cell apoptosis using MTT assay, as shown in Fig. 5b. It has been recognized that colon cancer cells are often capable of overexpressing P-glycoprotein (P-gp), one of the ABC transporters underlying the mechanism of multidrug resistance (MDR), on the surfaces of cell and nuclear membranes, leading to the high IC_{50} value (58 μM) of free DOX against CT26 cancer cells [52,53]. By contrast, the appreciable reduction of the IC_{50} values was observed for the DOX-loaded NPs, particularly FSLNs. As reported previously [54,55], TPGS (or TPGS conjugates) can act as a structural disturbing factor to cell membranes, leading to conformational change of P-gp and inhibition of the required ATPase activity. The FLSNs showed the lowest IC_{50} value

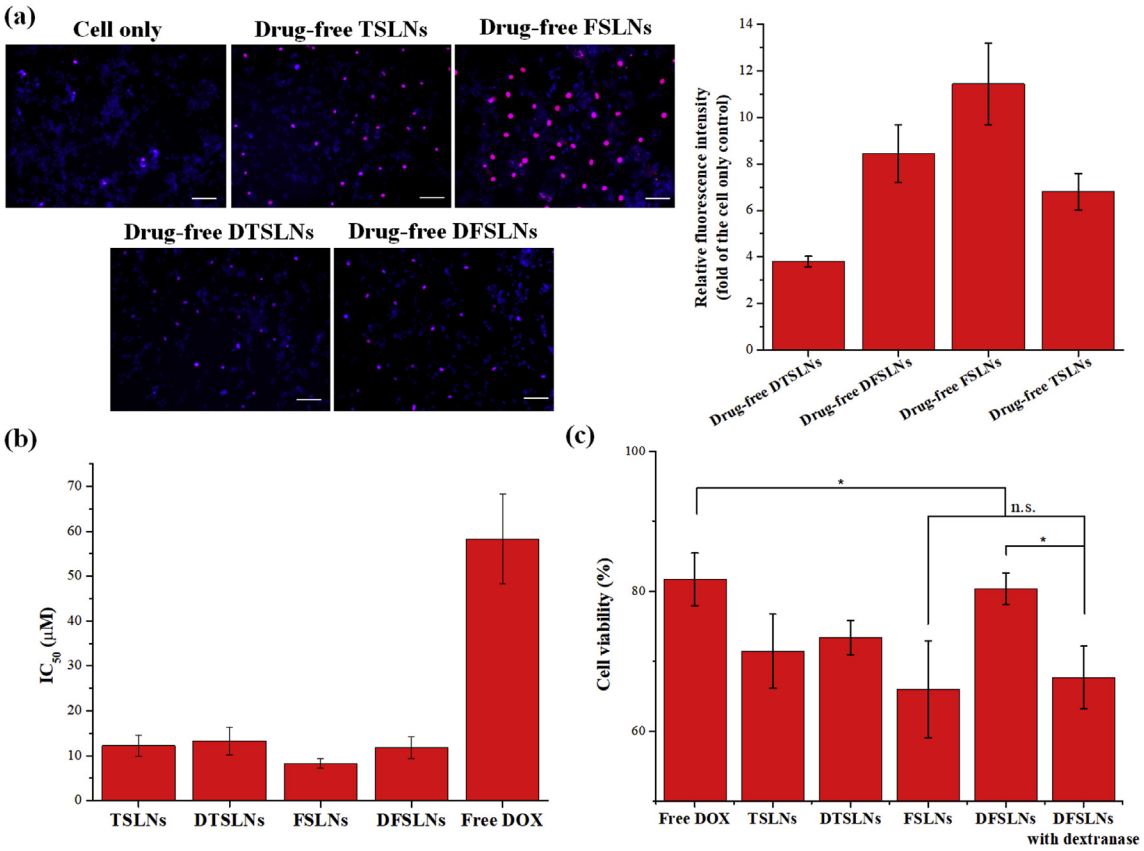

Fig. 5. *In vitro* therapeutic effects of hyperthermia, chemotherapy and combination therapy. (a) Fluorescence images of necrotic CT26 cells via Hoechst 33342/PI double staining. CT26 cells were incubated with various drug-free SLNs for 4 h, followed by HFMF treatment for 7 min. Scale bars are 100 μm. The average fluorescence intensity was analyzed by Image J (n = 10). (b) IC_{50} values of various SLNs on CT26 cells. The IC_{50} value was obtained from the cell viability data of chemotherapy by MTT assay (n = 8). (c) Cell viability of CT26 cells treated with combination therapy at the DOX concentration of 5 μM by MTT assay (n = 6). Samples were analyzed with one-way ANOVA, followed by Bonferroni correction for multiple comparisons. *$P < 0.05$ and n.s. $P > 0.05$. Error bars represent mean ± s.d.

owing to the enhanced uptake by CT26 cells via the FAR-mediated effect. Fig. 5c shows the cytotoxic effect from the combination of chemotherapy with magnetothermal therapy of the SLNs against CT26 cancer cells as examined by MTT assay. The DOX concentration of 5.0 μM in all NP formulations was adopted while the HFMF treatment was performed for 7 min. In contrast to free DOX showing limited cytotoxicity due to the low concentration employed, the viability of the CT26 cancer cells receiving SLNs was appreciably reduced by hyperthermia ablation alongside the TPGS effect on P-gp ATPase inhibition as aforementioned to enhance chemotherapeutic efficacy. As expected, the most profound cytotoxicity of the combination therapy against the cancer cells was found for the treatment with FSLNs and dextranase-pretreated DFSLNs due to the facilitated cellular uptake of the NPs by means of the FAR-receptor mediated endocytosis. Meanwhile, the combination index (CI) values of dextranase-pretreated DTSLNs and DFSLNs with the DOX concentration of 5.0 μM were calculated with CompuSyn software. The CI values of 0.48 and 0.21 for DTSLNs and DFSLNs (Fig. S12), respectively, indicate a synergistic effect (CI < 1) of the combination therapy as reported previously [42]. The difference in the values (0.48 for DTSLNs and 0.21 for DFSLNs) also imply that the folate targeting of DFSLNs plays an essential role in the synergistic effect of the combination therapy as compared to DTSLNs most probably by the enhanced cellular uptake of DFSLNs via FAR-mediated endocytosis.

3.4. *In vivo* NP distribution in GI tract and therapeutic efficacy

The *in vivo* performance of the hierarchically targeting DFSLNs in terms of the distribution along the GI tract, tumor accumulation, antitumor efficacy, and anti-metastatic effect was further investigated. The ex vivo imaging of small intestine and colon (including rectum) harvested from the CT26 tumor-bearing BALB/c mice at 6 h after the gavage of various DiI-labeled SLNs is shown in Fig. 6a. DiI was used as a hydrophobic fluorescence probe for IVIS detection. The accumulation of FSLNs in small intestine was the most significant among all SLN formulations though a considerable amount of FSLNs in colon was also observed. The enhanced residence of FSLNs in small intestinal region was ascribed to the recognition of the FA residues on NP surfaces by the proton-coupled folate transporters on the apical brush-border membrane of the small intestine [56]. By contrast, the FA residues were sequestered by the dextran coating on DFSLNs, thus reducing the accumulation of DFSLNs in intestine. Owing to the absence of FA and dextran on surfaces for hierarchical targeting, the quantities of TSLNs within small intestine and colon were considerably reduced. Fig. 6b further shows the accumulation of various SLNs in the colon tumor region. Surprisingly, the tumor accumulation of FSLNs was lower than that of TSLNs, implying strongly the significant FA binding with its transporters in small intestine. These results warrant the need to protect the FA residues from the recognition by the transporters. The dextran coating on the surface of DFSLNs promoted the targeting of the NPs to colon at least 2 folds, in part by evading the undesired biorecognition and capturing on the brush-border membranes of the small intestine. Compared to the difference between DFSLNs and FSLNs, the difference in the tumor accumulation between DTSLNs and TSLNs was reduced because of the lack of FA residues on specific binding with FAR of cancer cells.

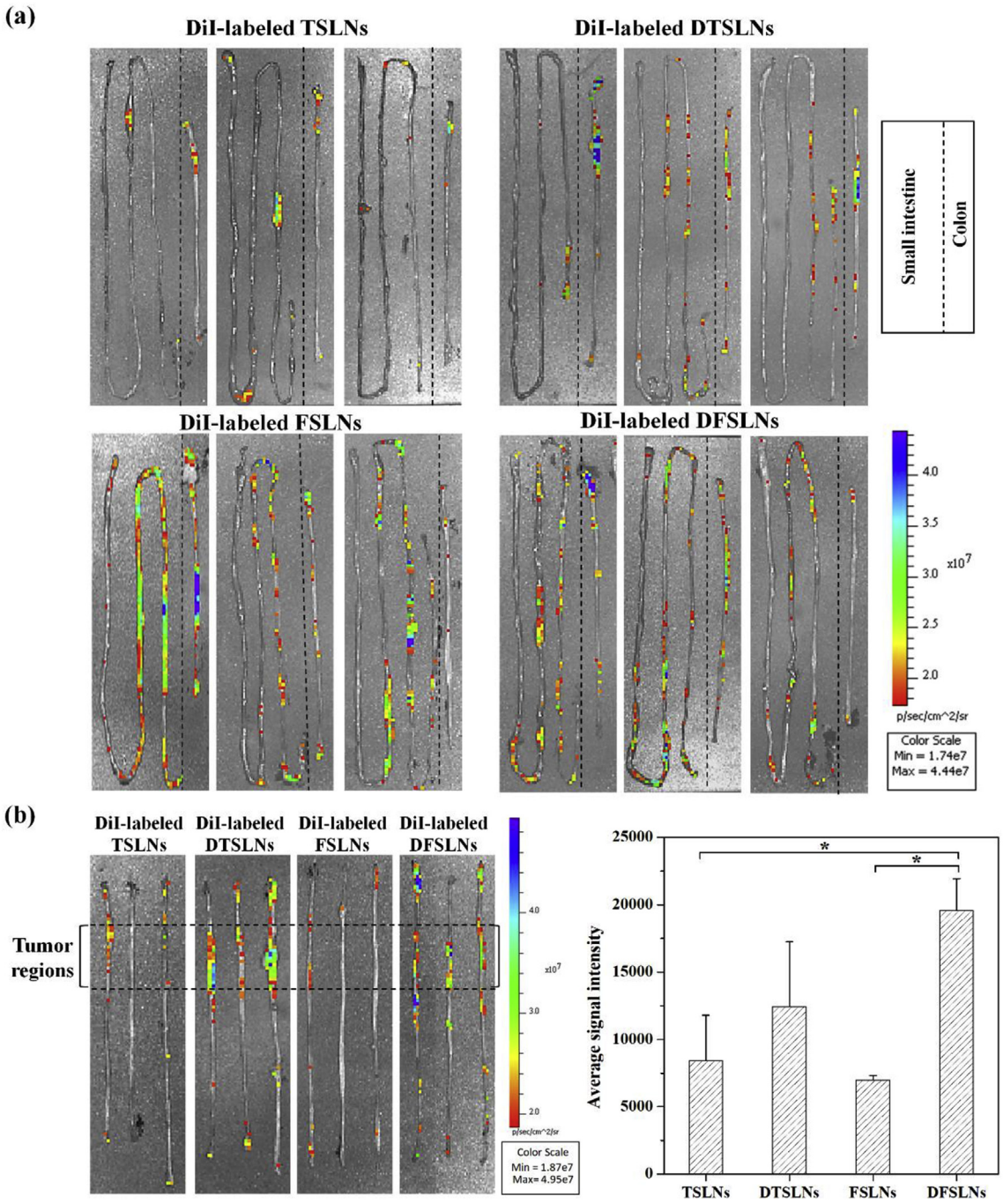

Fig. 6. Ex vivo fluorescence images of (a) small intestine and colon collected from orthotopic CT26 tumor-bearing mice at 6 h after the gavage of various SLNs. DiI was used to label the nanoparticles for fluorescent detection. (b) Accumulation of DiI-labeled SLNs within the tumor region via IVIS imaging. The average signal intensity was obtained from the fluorescence signal intensity of ROIs in the images. Samples were analyzed with unpaired two-tailed *t*-test. $^*P < 0.05$. Error bars represent mean ± s.d (n = 3).

The LSCM examination of small intestine and colon tissue sections from the tumor-bearing mice at 6 h after the gavage of various DiI-labeled SLNs was performed and the IOD of DiI was obtained by analyzing the fluorescence images from 10 randomly selected tissue sections. The results (Fig. S13a and b) reveal that, among various SLN formulations, the FSLNs exhibited the most intense fluorescence signals as well as the highest IOD value in small intestine, indicating that the FSLNs were significantly captured by FA transporters on brush border membranes in small intestine. By contrast, the fluorescence intensity of DiI-labeled DFSLNs in colon tumor tissue sections was significantly enhanced, at least 4 folds higher than that of other SLN formulations. In agreement with the ex-vivo fluorescence imaging of small intestine and colon by IVIS (Fig. 6), the data further confirm the success of the strategy on hierarchical dual-targeting that significantly enhances the accumulation of DFSLNs in the colorectal tumor. On the other hand, the ex-vivo biodistribution evaluation showed negligible accumulations of DTSLNs and DFSLNs in major organs (Fig. S13c), thereby indicating very low drug absorption occurring during the treatment. To further evaluate the DOX levels in the colorectal normal and tumor regions, DOX was extracted from the tissues with HCl/propanol solution after the colon contents being fully removed. The results as illustrated in Fig. 7 demonstrate the highest DOX concentration found in the colon

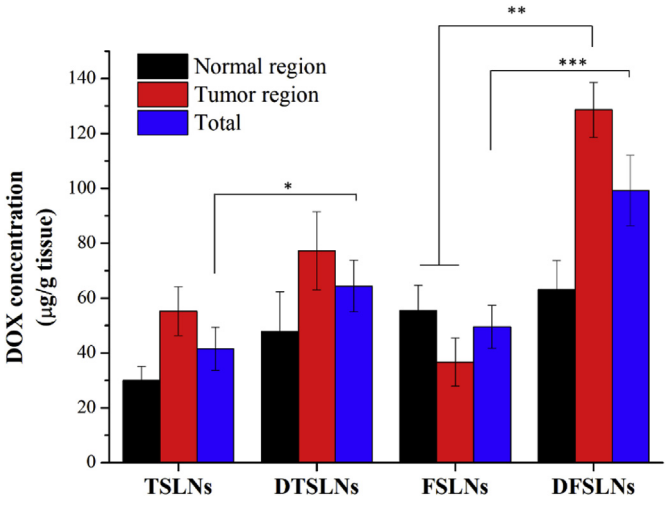

Fig. 7. DOX amounts in the normal, tumor and entire areas of colon tissues from orthotopic colon tumor-bearing mice receiving TSLNs, FSLNs, DTSLNs and DFSLNs by gavage, respectively. Samples were analyzed with one-way ANOVA, followed by Bonferroni correction for multiple comparisons. $^{***}P < 0.001$, $^{**}P < 0.01$ and $^{*}P < 0.05$. Error bars represent mean ± s.d (n = 3).

(including normal and tumor regions) with the DFSLNs treatment as compared to other formulations and the amount of DFSLNs in tumor was significantly higher than that in normal region. These results again indicate that the dextran coating and FA decorating on SLN surfaces indeed improve the selective accumulation within the colorectal tumor site.

The *in vivo* therapeutic efficacy of various SLN formulations was further investigated in terms of the growth inhibition of orthotopic colon tumor and pcCRC from the orthotopic colon tumor-bearing mice. The latter was evaluated as the anti-metastasis effect of the SLN treatment on colon cancer by oral administration. The tumor-bearing mice received free DOX, TSLNs, FSLNs and DFSLNs, respectively, by oral gavage daily for three days starting on day 5 post-implantation of CT26 cancer cells. The HFMF treatment was performed 6 h after each gavage. The tumor-bearing mice were sacrificed at day 14 after the first SLN treatment and the tumor sizes were evaluated from the harvested colon. Fig. 8a shows the photographs of the tumor-bearing colon sections after the treatments. The tumors receiving both DFSLNs and HFMF treatments were the smallest in size among all others, although the tumor volume varied greatly among individual mice. Compared with the PBS control, a 15-fold decrease in tumor mass of mice receiving the DFSLNs/HFMF treatment undoubtedly illustrates the prominent tumor growth inhibition capability of the chemo/thermal combination therapy (Fig. 8b). Without the HFMF treatment, DFSLNs also showed enhanced tumor inhibition with the tumor mass being decreased to less than one half of those from the FSLN and TSLN groups. Obviously, the antitumor effect of the SLNs was primarily governed by the accumulation of SLNs at tumor and the uptake by cancer cells. Owing to the dual targeting approach adopted herein in a hierarchical manner, DFSLNs not only reduce the cellular penetration through brush border membranes mediated by proton-coupled FA transporters in small intestine, but also enhance the residing duration in colon and thus cellular entry into colon cancer cells.

As revealed by H&E staining of the tumor tissues (Fig. 9), the tissue sections receiving PBS, free DOX, TSLNs and TSLNs/HFMF showed typical tumor characteristics, including the tumor invasion in colorectal walls and the disrupted structure of colon mucosa. In Fig. 9, the tumor regions were indicated by yellow stars and the tumor-invasive colon mucosa were highlighted by red arrows. By contrast, upon DFSLNs/HFMF treatments, the tissue section showed limited tumor regions alongside the well-preserved mucosa structure at the tumor invasive fronts, indicating a prominent therapeutic efficacy from the treatment. As for the DFSLNs treatment alone, the tumor regions were somewhat enlarged although the mucosa structure appeared intact at the invasive fronts from the H&E staining. Further examination of the therapeutic efficacy from various SLN treatments was performed by the IHC staining of caspase 3, a key protein indicator essentially involved in the apoptosis pathway, of tumor tissues. As shown in Fig. 10a, the most profound signal intensity of the caspase 3 marker was found for the tumor tissue receiving DFSLNs/HFMF treatment. By comparing the caspase signal intensity in tissues between the SLNs and the SLNs/HFMF groups, the effect of HFMF on cell death could be assessed. As reported previously, hyperthermia not only induces cell necrosis, but also sub-lethal damages and subsequent apoptosis of tumor cells in the peripheral areas of the treatment [57,58]. Fig. 10b shows the cell apoptosis of the intestine tissue sections after the treatment. The significantly increased apoptosis occurred for the FSLNs treatment in combination with magnetothermal therapy in small intestine. This is ascribed to the enhanced accumulation of FSLNs via complementary binding of FA residues with FA transporter on brush border membranes. By contrast, owing to the shielding effect of the dextran coating on DFSLN surfaces, the cell apoptosis was appreciably reduced after the treatment, owing to the decreased accumulation in small intestine.

As aforementioned, the orthotopic colon tumor model in this study was established by the injection of CT26 cancer cells into mice colon walls. It is thus expectable that the pcCRC can easily occur in the tumor-bearing mice via the penetration of cancer cells through colon walls. The growth inhibition of pcCRC, also a measure of the therapeutic efficacy, in tumor-bearing mice after the SLNs/HFMF treatment was

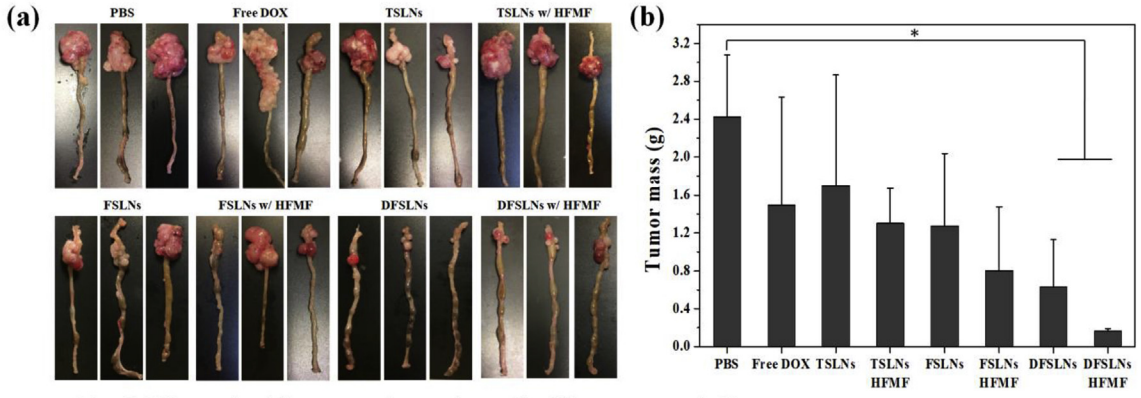

Fig. 8. (a) Photographs of the tumor-bearing colon in each treated group harvested from the mice sacrificed at day 14 post treatment (the end point). (b) Average tumor mass of each group harvested from tumor-bearing mice at day 14 post treatment. Samples were analyzed with unpaired two-tailed *t*-test (n = 3, $^{*}P < 0.05$, error bars represent mean ± s.d).

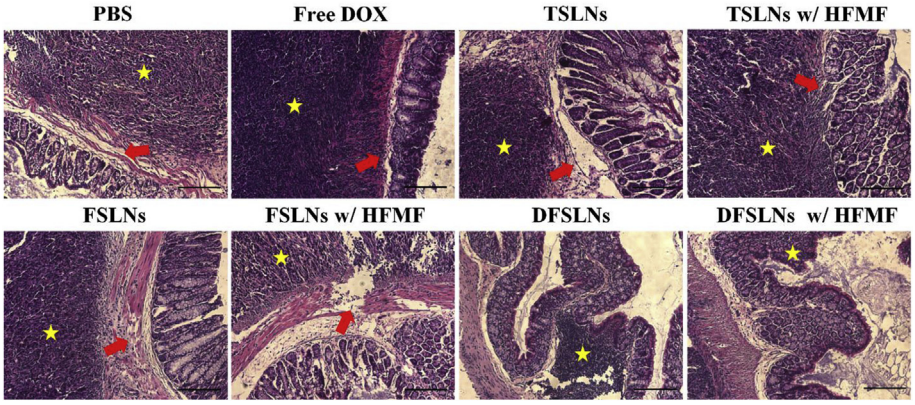

Fig. 9. H&E examination of tumor sections harvested from tumor-bearing mice at the end point of the treatments. Yellow stars symbolize the tumor regions and red arrows the tumor-invasive colon mucosa. Scale bars are 150 μm. (For interpretation of the references to color in this figure legend, the reader is referred to the Web version of this article.)

evaluated. Fig. 11a illustrates the tumors in peritoneal cavity with the surgery applied on the mice receiving various treatments. In Fig. 11a, the yellow empty circles were used for tumor identification. In agreement with the therapeutic data in orthotopic colon tumor inhibition, the tumor nodule number and size of pcCRC shown in the photographs were considerably reduced for the mice treated with DFSLNs or DFSLNs/HFMF. The levels of ascites and tumor nodules and the MCI score, representing the degree of pcCRC in a quantitative manner, were

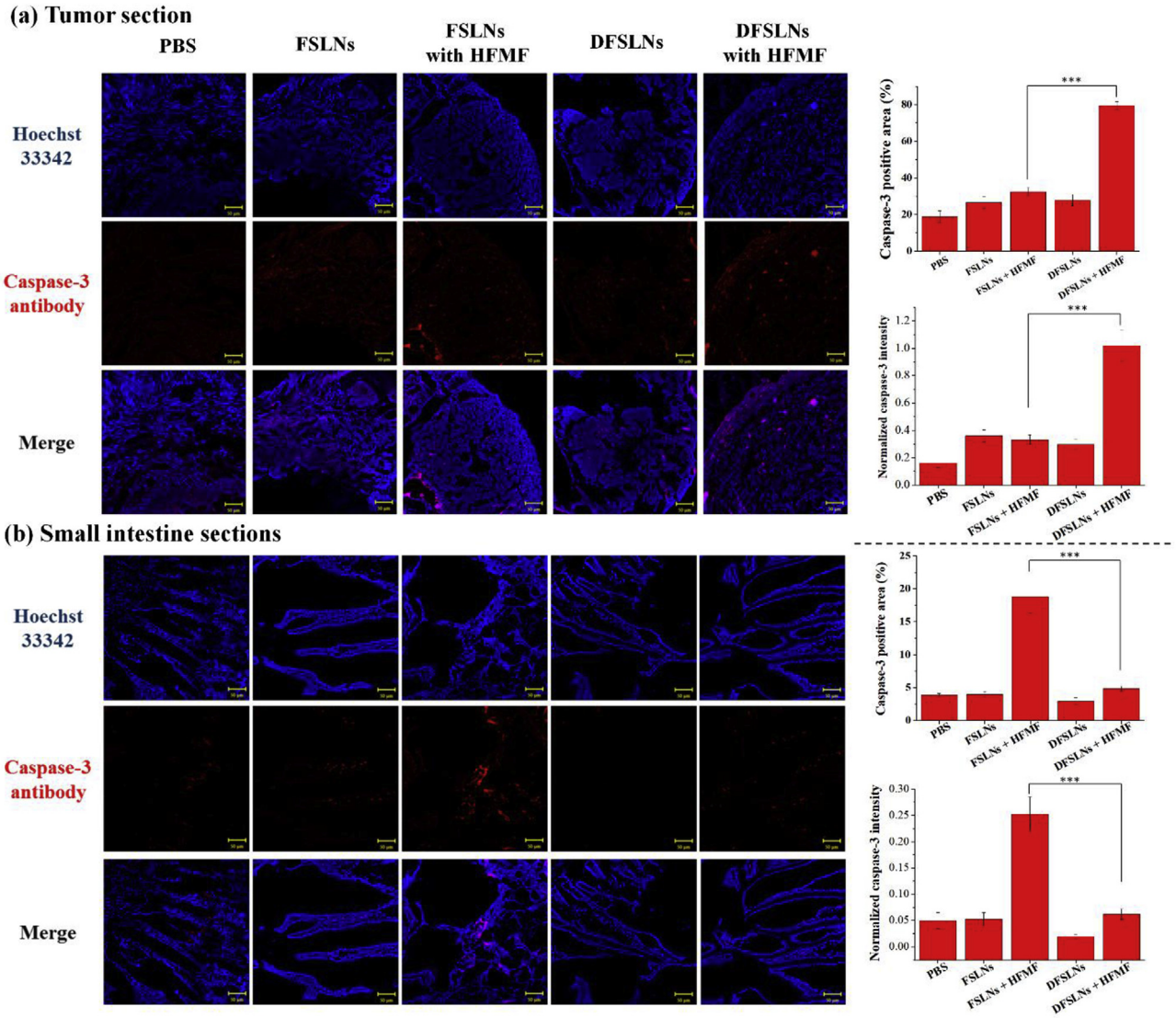

Fig. 10. Fluorescence images and quantification analyses of (a) tumor and (b) small intestine sections harvested from tumor-bearing mice at day 14 after treatments. Cell nuclei and apoptosis were stained with Hoechst 33342 (blue) and caspase-3 marker (red), respectively. Scale bars are 50 μm. The data were analyzed by one-way ANOVA with Bonferroni multiple comparison post-test. ***P $<$ 0.001. Error bars represent mean $\pm$ s.d (n = 10). (For interpretation of the references to color in this figure legend, the reader is referred to the Web version of this article.)

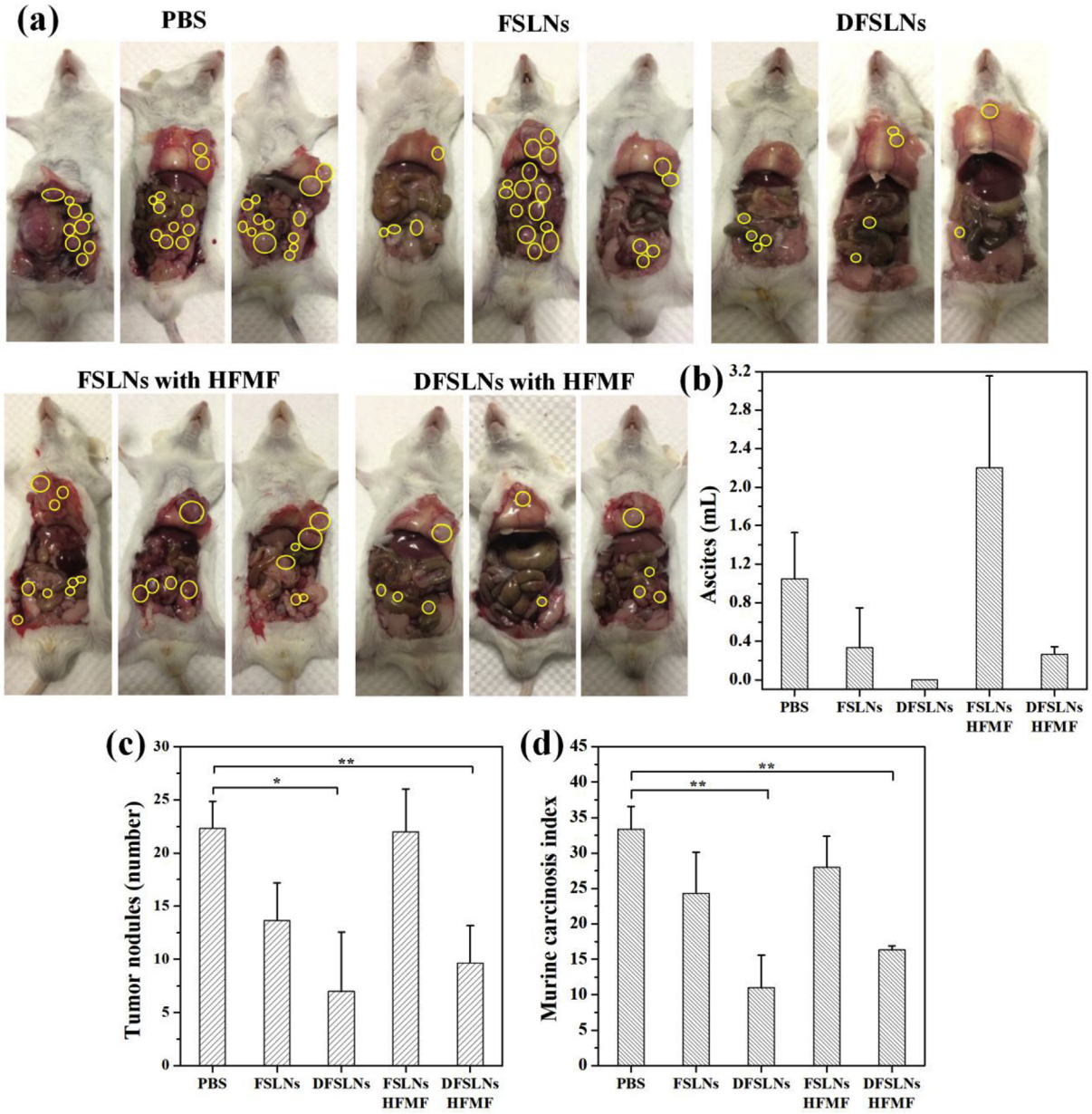

Fig. 11. Evaluation of the tumor metastasis inhibition of pcCRC at the end point of the treatments. (a) Surgical photographs of animal peritoneal cavity. Yellow circles signify the tumor nodules. (b–d) Ascites volume, tumor nodule number and MCI score evaluated from mouse peritoneal cavity in each experimental group. Samples were analyzed with unpaired two-tailed *t*-test. $^{**}P < 0.01$, $^{*}P < 0.05$. Error bars represent mean ± s.d (n = 3). (For interpretation of the references to color in this figure legend, the reader is referred to the Web version of this article.)

illustrated in Fig. 11b–d. For the mice receiving DFSLNs with and without the HFMF treatment, the amount of ascites collected and the number of tumor nodules were both significantly reduced, strongly suggesting the pronounced therapeutic efficacy of the SLNs equipped with hierarchical, dual targeting devices. The DFSLN treatment gave an MCI score, a combination index of tumor number and size of pcCRC, only one third of the PBS control group, suggesting the effective inhibition of metastasis (Fig. 11d). Although the differences were not statistically significant, primarily owing to the considerable variation in pcCRC among individual mice in each group, it is noteworthy that the levels of ascites and the number of tumor nodules were higher with the combination therapy, compared to those only with the SLNs treatment in the absence of HFMF. Although the reasons are not yet clear, it could be a result of local tissue damage, leading to facilitated cancer cell migration and promoted inflammation [59,60]. Nevertheless, the pronounced antitumor effect of the DFSLNs and DFSLNs/HFMF treatments on orthotopic colon tumor-bearing mice by oral administration was observed from both the effective growth inhibition of primary colon cancer and the substantial reduction of nodule number and size of pcCRC.

In addition to the therapeutic efficacy examination, it is also important to evaluate the systemic toxicity of the therapeutic approach developed in this work. Blood samples were collected from orbital sinus of tumor-bearing mice at day 7 and 14 after receiving the first SLN treatment. As shown in Fig. S14, the liver function index, represented by the ALP/ALT ratio, of the mice receiving various treatments were in the normal range, typically ca. 2 to 4 for healthy mice [61,62], indicating that the oral delivery strategy of the SLN formulations did not cause severe hepatic damage, most probably due to the reduced drug adsorption into systemic circulation. The body weight of the tumor-bearing mice after therapeutic treatments were found relatively unchanged during a period of 14 days, most likely a result of the absence

of the systemic side effects with the treatments (Fig. S15a). Besides, the H&E staining of the tissue sections of the harvested major organs showed no obvious tissue damages (Fig. S15b). All these preliminary results suggested the lack of the systemic toxicity and the safety of the NPs formulations for the oral administration.

4. Conclusions

The selective, enhanced accumulation of the DOX/SPIONs-loaded DFSLNs at colon tumor sites confirmed the successful development of a hierarchical and dual targeting SLN formulations for the oral delivery of dual modality local therapy against colon cancer. The SLNs decorated with FA residues and coated with dextran shell layer cannot only evade the cellular transport and systemic absorption via avoiding biorecognition by with the proton-coupled FA transporters located on brush border membrane surfaces in small intestine, but also enhance the accumulation in colon by the specific association of dextran with dextranase present exclusively in colon. Upon the enzymatic degradation and removal of the dextran shells, the targeting of the SLNs to tumor on the cellular level was achieved by the complementary binding with the FAR-overexpressed CT26 colon cancer cells, leading to the facilitated cellular uptake of the DFSLNs by the cancer cells via the FAR-mediated endocytosis and the pronounced antitumor performance of the chemo/magnetothermal combination therapy of the SLN formulations both *in vitro* and *in vivo*. In particular, the effective tumor growth inhibition of the orthotopic colon tumor and the substantial reduction of the nodule number and size of pcCRC for the tumor-bearing mice receiving the DFSLNs and DFSLNs/HFMF treatments, respectively, clearly demonstrated the prominent therapeutic efficacy of DFSLNs for local treatment(s) by oral administration. Because of the restricted therapeutic action of the dual-targeted DFSLN therapy delivery system on the local tumor sites, no apparent systemic side effects were observed.

Conflict of interest

The authors declare no competing financial interest.

Declarations of interest

None.

Data availability statement

The raw/processed data required to reproduce these findings cannot be shared at this time due to technical or time limitations. Data will be made available on request.

Acknowledgments

This work was supported by the Ministry of Science and Technology, Taiwan (MOST 106-2221-E-002-075-); the National Taiwan University Hospital (107-HCH037); the National Tsing Hua University (107Q2521E1); and the Mackay Memorial Hospital (MMH-TH-10702).

Appendix A. Supplementary data

Supplementary data to this article can be found online at https://doi.org/10.1016/j.biomaterials.2019.01.019.

References

[1] K.D. Miller, R.L. Siegel, C.C. Lin, A.B. Mariotto, J.L. Kramer, J.H. Rowland, K.D. Stein, R. Alteri, A. Jemal, Cancer treatment and survivorship statistics, 2016, Ca-Cancer, J. Clin. 66 (4) (2016) 271–289.
[2] B. Gustavsson, G. Carlsson, D. Machover, N. Petrelli, A. Roth, H.J. Schmoll, K.M. Tveit, F. Gibson, A review of the evolution of systemic chemotherapy in the management of colorectal cancer, Clin. Colorectal Canc. 14 (1) (2015) 1–10.
[3] K.K. Ciombor, C. Wu, R.M. Goldberg, Recent therapeutic advances in the treatment of colorectal cancer, Annu. Rev. Med. 66 (2015) 83–95.
[4] J. Maroun, H. Marginean, D. Jonker, C. Cripps, R. Goel, T. Asmis, R. Goodwin, G. Chiritescu, A phase I study of irinotecan, capecitabine (Xeloda), and oxaliplatin in patients with advanced colorectal cancer, Clin. Colorectal Canc. 17 (2) (2018) e257–e268.
[5] J. Sakamoto, C. Hamada, S. Yoshida, S. Kodaira, M. Yasutomi, T. Kato, K. Oba, H. Nakazato, S. Saji, Y. Ohashi, An individual patient data meta-analysis of adjuvant therapy with uracil-tegafur (UFT) in patients with curatively resected rectal cancer, Br. J. Canc. 96 (8) (2007) 1170–1177.
[6] K. Maisel, L. Ensign, M. Reddy, R. Cone, J. Hanes, Effect of surface chemistry on nanoparticle interaction with gastrointestinal mucus and distribution in the gastrointestinal tract following oral and rectal administration in the mouse, J. Contr. Release 197 (2015) 48–57.
[7] L.M. Ensign, R. Cone, J. Hanes, Oral drug delivery with polymeric nanoparticles: the gastrointestinal mucus barriers, Adv. Drug Deliv. Rev. 64 (6) (2012) 557–570.
[8] J.C. Kolars, W.M. Awni, R.M. Merion, P.B. Watkins, First-pass metabolism of cyclosporin by the gut, Lancet 338 (8781) (1991) 1488–1490.
[9] G. Bocci, R.S. Kerbel, Pharmacokinetics of metronomic chemotherapy: a neglected but crucial aspect, Nat. Rev. Clin. Oncol. 13 (11) (2016) 659–673.
[10] R. Zhang, K. Cheng, A.L. Antaris, X. Ma, M. Yang, S. Ramakrishnan, G. Liu, A. Lu, H. Dai, M. Tian, Z. Cheng, Hybrid anisotropic nanostructures for dual-modal cancer imaging and image-guided chemo-thermo therapies, Biomaterials 103 (2016) 265–277.
[11] Y. Li, C. Jiang, D. Zhang, Y. Wang, X. Ren, K. Ai, X. Chen, L. Lu, Targeted polydopamine nanoparticles enable photoacoustic imaging guided chemo-photothermal synergistic therapy of tumor, Acta Biomater. 47 (2017) 124–134.
[12] B. Li, J. Tang, W. Chen, G. Hao, N. Kurniawan, Z. Gu, Z.P. Xu, Novel theranostic nanoplatform for complete mice tumor elimination via MR imaging-guided acid-enhanced photothermo-/chemo-therapy, Biomaterials 177 (2018) 40–51.
[13] M.M. Hasani-Sadrabadi, S. Taranejoo, E. Dashtimoghadam, G. Bahlakeh, F.S. Majedi, J.J. VanDersarl, M. Janmaleki, F. Sharifi, A. Bertsch, K. Hourigan, L. Tayebi, P. Renaud, K.I. Jacob, Microfluidic manipulation of core/shell nanoparticles for oral delivery of chemotherapeutics: a new treatment approach for colorectal cancer, Adv. Mater. 28 (21) (2016) 4134–4141.
[14] L.B. Vong, T. Yoshitomi, H. Matsui, Y. Nagasaki, Development of an oral nanotherapeutics using redox nanoparticles for treatment of colitis-associated colon cancer, Biomaterials 55 (2015) 54–63.
[15] L.B. Vong, Y. Nagasaki, Combination treatment of murine colon cancer with doxorubicin and redox nanoparticles, Mol. Pharm. 13 (2) (2016) 449–455.
[16] A. Gulbake, A. Jain, A. Jain, A. Jain, S.K. Jain, Insight to drug delivery aspects for colorectal cancer, World J. Gastroenterol. 22 (2) (2016) 582–599.
[17] S. Senapati, A.K. Mahanta, S. Kumar, P. Maiti, Controlled drug delivery vehicles for cancer treatment and their performance, Signal Transduct. Targeted Ther. 3 (1) (2018) 7.
[18] M.R. Schneider, M. Dahlhoff, D. Horst, B. Hirschi, K. Trulzsch, J. Muller-Hocker, R. Vogelmann, M. Allgauer, M. Gerhard, S. Steininger, E. Wolf, F.T. Kolligs, A key role for E-cadherin in intestinal homeostasis and paneth cell maturation, PLoS One 5 (12) (2010).
[19] A.I. Ivanov, A. Nusrat, C.A. Parkos, Endocytosis of epithelial apical junctional proteins by a clathrin-mediated pathway into a unique storage compartment, Mol. Biol. Cell 15 (1) (2004) 176–188.
[20] R.C. Schackmann, M. Tenhagen, R.A. van de Ven, P.W. Derksen, p120-catenin in cancer - mechanisms, models and opportunities for intervention, J. Cell Sci. 126 (16) (2013) 3515–3525.
[21] S. Hua, E. Marks, J.J. Schneider, S. Keely, Advances in oral nano-delivery systems for colon targeted drug delivery in inflammatory bowel disease: selective targeting to diseased versus healthy tissue, Nanomedicine 11 (5) (2015) 1117–1132.
[22] T.X. Nguyen, L. Huang, M. Gauthier, G. Yang, Q. Wang, Recent advances in liposome surface modification for oral drug delivery, Nanomedicine (Lond) 11 (9) (2016) 1169–1185.
[23] M. Fleming, S. Ravula, S.F. Tatishchev, H.L. Wang, Colorectal carcinoma: pathologic aspects, J. Gastrointest. Oncol. 3 (3) (2012) 153–173.
[24] D.W. Kufe, Mucins in cancer: function, prognosis and therapy, Nat. Rev. Canc. 9 (12) (2009) 874–885.
[25] W.H. Chiang, W.C. Huang, C.W. Chang, M.Y. Shen, Z.F. Shih, Y.F. Huang, S.C. Lin, H.C. Chiu, Functionalized polymersomes with out layered polyelectrolyte gels for potential tumor-targeted delivery of multimodal therapies and MR imaging, J. Contr. Release 168 (3) (2013) 280–288.
[26] C.C. Hung, W.C. Huang, Y.W. Lin, T.W. Yu, H.H. Chen, S.C. Lin, W.H. Chiang, H.C. Chiu, Active tumor permeation and uptake of surface charge-switchable theranostic nanoparticles for imaging-guided photothermal/chemo combinatorial therapy, Theranostics 6 (3) (2016) 302–317.
[27] J. Deng, S. Xu, W. Hu, X. Xun, L. Zheng, M. Su, Tumor targeted, stealthy and degradable bismuth nanoparticles for enhanced X-ray radiation therapy of breast cancer, Biomaterials 154 (2018) 24–33.
[28] M. Derrien, J.E.T.V. Vlieg, Fate, activity, and impact of ingested bacteria within the human gut microbiota, Trends Microbiol. 23 (6) (2015) 354–366.
[29] M.C. Costa, G. Silva, R.V. Ramos, H.R. Staempfli, L.G. Arroyo, P. Kim, J.S. Weese, Characterization and comparison of the bacterial microbiota in different gastrointestinal tract compartments in horses, Vet. J. 205 (1) (2015) 74–80.
[30] N. Naseri, H. Valizadeh, P. Zakeri-Milani, Solid lipid nanoparticles and nanostructured lipid carriers: structure, preparation and application, Adv. Pharmaceut. Bull. 5 (3) (2015) 305–313.

[31] A. Qiu, M. Jansen, A. Sakaris, S.H. Min, S. Chattopadhyay, E. Tsai, C. Sandoval, R. Zhao, M.H. Akabas, I.D. Goldman, Identification of an intestinal folate transporter and the molecular basis for hereditary folate malabsorption, Cell 127 (5) (2006) 917–928.
[32] R. Zhao, S.H. Min, Y. Wang, E. Campanella, P.S. Low, I.D. Goldman, A role for the proton-coupled folate transporter (PCFT-SLC46A1) in folate receptor-mediated endocytosis, J. Biol. Chem. 284 (7) (2009) 4267–4274.
[33] W.C. Huang, I.L. Lu, W.H. Chiang, Y.W. Lin, Y.C. Tsai, H.H. Chen, C.W. Chang, C.S. Chiang, H.C. Chiu, Tumortropic adipose-derived stem cells carrying smart nanotherapeutics for targeted delivery and dual-modality therapy of orthotopic glioblastoma, J. Contr. Release 254 (2017) 119–130.
[34] W.N.E. Vandijkwolthuis, O. Franssen, H. Talsma, M.J. Vansteenbergen, J.J.K. Vandenbosch, W.E. Hennink, Synthesis, characterization, and polymerization of glycidyl methacrylate derivatized dextran, Macromolecules 28 (18) (1995) 6317–6322.
[35] W.N.E. vanDijkWolthuis, S.K.Y. Tsang, J.J. KettenesvandenBosch, W.E. Hennink, A new class of polymerizable dextrans with hydrolyzable groups: hydroxyethyl methacrylated dextran with and without oligolactate spacer, Polymer 38 (25) (1997) 6235–6242.
[36] S.C. De Smedt, A. Lauwers, J. Demeester, M.J. Vansteenbergen, W.E. Hennink, S.P.F.M. Roefs, Characterization of the network structure of dextran glycidyl methacrylate hydrogels by studying the rheological and swelling behavior, Macromolecules 28 (14) (1995) 5082–5088.
[37] W.H. Chiang, Y.J. Lan, Y.C. Huang, Y.W. Chen, Y.F. Huang, S.C. Lin, C.S. Chern, H.C. Chiu, Multi-scaled polymersomes from self-assembly of octadecanol-modified dextrans, Polymer 53 (11) (2012) 2233–2244.
[38] H.C. Chiu, T. Hsiue, W.Y. Chen, FTIR-ATR measurements of the ionization extent of acrylic acid within copolymerized methacrylated dextran/acrylic acid networks and its relation with pH/salt concentration-induced equilibrium swelling, Polymer 45 (5) (2004) 1627–1636.
[39] H.C. Chiu, Y.F. Lin, S.H. Hung, Equilibrium swelling of copolymerized acrylic acid-methacrylated dextran networks: effects of pH and neutral salt, Macromolecules 35 (13) (2002) 5235–5242.
[40] M.R.C. Marques, R. Loebenberg, M. Almukainzi, Simulated biological fluids with possible application in dissolution testing, Dissolution Technol. 18 (3) (2011) 15–28.
[41] C. Feng, R.X. Song, G.H. Sun, M. Kong, Z.X. Bao, Y. Li, X.J. Cheng, D. Cha, H. Park, X.G. Chen, Immobilization of coacervate microcapsules in multilayer sodium alginate beads for efficient oral anticancer drug delivery, Biomacromolecules 15 (3) (2014) 985–996.
[42] T.-C. Chou, Drug combination studies and their synergy quantification using the chou-talalay method, 70 (2) (2010) 440–446.
[43] W. Tseng, X. Leong, E. Engleman, Orthotopic mouse model of colorectal cancer, J. Vis. Exp. 10 (2007) 484.
[44] Z. Liu, A.C. Fan, K. Rakhra, S. Sherlock, A. Goodwin, X. Chen, Q. Yang, D.W. Felsher, H. Dai, Supramolecular stacking of doxorubicin on carbon nanotubes for in vivo cancer therapy, Angew. Chem. 121 (41) (2009) 7804–7808.
[45] L. Picaud, B. Thibault, E. Mery, M. Ouali, A. Martinez, J.P. Delord, B. Couderc, G. Ferron, Evaluation of the effects of hyaluronic acid-carboxymethyl cellulose barrier on ovarian tumor progression, J. Ovarian Res. 7 (2014) 40.
[46] O. Franssen, R.D. van Ooijen, D. de Boer, R.A.A. Maes, W.E. Hennink, Enzymatic degradation of cross-linked dextrans, Macromolecules 32 (9) (1999) 2896–2902.
[47] O. Franssen, R.D. vanOoijen, D. deBoer, R.A.A. Maes, J.N. Herron, W.E. Hennink, Enzymatic degradation of methacrylated dextrans, Macromolecules 30 (24) (1997) 7408–7413.
[48] F. Chen, Y.X. Xing, Z.Q. Wang, X.Y. Zheng, J.X. Zhang, K.Y. Cai, Nanoscale polydopamine (PDA) meets pi-pi interactions: an interface-directed coassembly approach for mesoporous nanoparticles, Langmuir 32 (46) (2016) 12119–12128.
[49] P. Huang, C. Xu, J. Lin, C. Wang, X.S. Wang, C.L. Zhang, X.J. Zhou, S.W. Guo, D.X. Cui, Folic acid-conjugated graphene oxide loaded with photosensitizers for targeting photodynamic therapy, Theranostics 1 (2011) 240–250.
[50] S.A. Kamba, M. Ismail, S.H. Hussein-Al-Ali, T.A.T. Ibrahim, Z.A. Zakaria, In Vitro Delivery and controlled release of doxorubicin for targeting osteosarcoma bone cancer, Molecules 18 (9) (2013) 10580–10598.
[51] S. Xu, B.Z. Olenyuk, C.T. Okamoto, S.F. Hamm-Alvarez, Targeting receptor-mediated endocytotic pathways with nanoparticles: rationale and advances, Adv. Drug Deliv. Rev. 65 (1) (2013) 121–138.
[52] W. Szaflarski, P. Sujka-Kordowska, R. Januchowski, K. Wojtowicz, M. Andrzejewska, M. Nowicki, M. Zabel, Nuclear localization of P-glycoprotein is responsible for protection of the nucleus from doxorubicin in the resistant LoVo cell line, Biomed. Pharmacother. 67 (6) (2013) 497–502.
[53] K. Ogawara, K. Un, K. Tanaka, K. Higaki, T. Kimura, In vivo anti-tumor effect of PEG liposomal doxorubicin (DOX) in DOX-resistant tumor-bearing mice: involvement of cytotoxic effect on vascular endothelial cells, J. Contr. Release 133 (1) (2009) 4–10.
[54] E.M. Collnot, C. Baldes, U.F. Schaefer, K.J. Edgar, M.F. Wempe, C.M. Lehr, Vitamin E TPGS P-glycoprotein inhibition mechanism: influence on conformational flexibility, intracellular ATP levels, and role of time and site of access, Mol. Pharm. 7 (3) (2010) 642–651.
[55] J.M. Dintaman, J.A. Silverman, Inhibition of P-glycoprotein by D-alpha-tocopheryl polyethylene glycol 1000 succinate (TPGS), Pharm. Res. 16 (10) (1999) 1550–1556.
[56] M. Visentin, N. Diop-Bove, R. Zhao, I.D. Goldman, The intestinal absorption of folates, Annu. Rev. Physiol. 76 (2014) 251–274.
[57] A.C. Silva, T.R. Oliveira, J.B. Mamani, S.M. Malheiros, L. Malavolta, L.F. Pavon, T.T. Sibov, E. Amaro Jr., A. Tannus, E.L. Vidoto, M.J. Martins, R.S. Santos, L.F. Gamarra, Application of hyperthermia induced by superparamagnetic iron oxide nanoparticles in glioma treatment, Int. J. Nanomed. 6 (2011) 591–603.
[58] K.F. Chu, D.E. Dupuy, Thermal ablation of tumours: biological mechanisms and advances in therapy, Nat. Rev. Canc. 14 (3) (2014) 199–208.
[59] A. Kuraishy, M. Karin, S.I. Grivennikov, Tumor promotion via injury- and death-induced inflammation, Immunity 35 (4) (2011) 467–477.
[60] S. Shalapour, M. Karin, Immunity, inflammation, and cancer: an eternal fight between good and evil, J. Clin. Invest. 125 (9) (2015) 3347–3355.
[61] L. O'Connor, A.W. Harris, A. Strasser, CD95 (Fas/APO-1) and p53 signal apoptosis independently in diverse cell types, Cancer Res. 60 (5) (2000) 1217–1220.
[62] Z.Y. He, F. Deng, X.W. Wei, C.C. Ma, M. Luo, P. Zhang, Y.X. Sang, X. Liang, L. Liu, H.X. Qin, Y.L. Shen, T. Liu, Y.T. Liu, W. Wang, Y.J. Wen, X. Zhao, X.N. Zhang, Z.Y. Qian, Y.Q. Wei, Ovarian cancer treatment with a tumor-targeting and gene expression-controllable lipoplex, Sci. Rep. 6 (2016) 23764.